Cirrus Cloud Properties and the Large-Scale Meteorological Environment: Relationships Derived from A-Train and NCEP–NCAR Reanalysis Data

ELIZABETH BERRY AND GERALD G. MACE

University of Utah, Salt Lake City, Utah

(Manuscript received 6 April 2012, in final form 26 November 2012)

ABSTRACT

Empirical knowledge of how cirrus cloud properties are coupled with the large-scale meteorological environment is a prerequisite for understanding the role of microphysical processes in the life cycle of cirrus cloud systems. Using active and passive remote sensing data from the A-Train, relationships between cirrus cloud properties and the large-scale dynamics are examined. Mesoscale cirrus events from along the A-Train track from 1 yr of data are sorted on the basis of vertical distributions of radar reflectivity and on large-scale meteorological parameters derived from the NCEP–NCAR reanalysis using a *K*-means cluster-analysis algorithm. With these defined regimes, the authors examine two questions: Given a cirrus cloud type defined by cloud properties, what are the large-scale dynamics? Vice versa, what cirrus cloud properties tend to emerge from large-scale dynamics regimes that tend to form cirrus? From the answers to these questions, the links between the large-scale dynamics regimes and the genre of cirrus that evolve within these regimes are identified. It is found that, to a considerable extent, the large-scale environment determines the bulk cirrus properties and that, within the dynamics regimes, cirrus cloud systems tend to evolve through life cycles, the details of which are not necessarily explained by the large-scale motions alone. These results suggest that, while simple relationships may be used to parameterize the gross properties of cirrus, more sophisticated parameterizations are required for representing the detailed structure and radiative feedbacks of these clouds.

1. Introduction

Differences in cloud feedback have been noted as the dominant source of uncertainty in global climate model (GCM) projections (Soden and Vecchi 2011; Soden and Held 2006; Dufresne and Bony 2008). Notable is that it has been shown that the largest source of intermodel variability in cloud feedbacks is due to low-level clouds (Webb et al. 2006; Bony and Dufresne 2005; Soden and Vecchi 2011). Although the intermodel variability in shortwave and longwave cloud feedbacks for high clouds can be large, these feedbacks tend to cancel each other out so that the intermodal variability in net cloud feedback due to high clouds is small relative to low clouds (Zelinka et al. 2012). These results suggest that simulated high-level clouds are not contributing significantly to the variability in projected climate sensitivity in terms of the net cloud feedback in the generation of GCMs used in the Intergovernmental Panel on Climate Change Fourth Assessment Report (AR4). Yet Sanderson et al. (2008) looked at more than a dozen feedback parameters responsible for variation in response to greenhouse gas forcing and found that the ice fall speed was the second greatest contributor to model sensitivity.

In terms of cloud radiative effect, Soden and Vecchi (2011) show that high-level clouds, through their reduction of infrared emission to space, impose a significant positive radiative forcing in the upper troposphere, especially in the tropics. Changes to high-level clouds also contribute to the positive feedback that clouds overall impose on the climate system. Of interest is that, among the ensemble of models, there is a consistent change in high-cloud forcing during climate change simulations, resulting in a similar change in radiative forcing. Because the feedback factor used for model diagnostics is essentially defined as the change in radiative forcing from a reference climate normalized by the change in global temperature (Soden and Held 2006), this consistent change in high-cloud forcing across the model ensemble

Corresponding author address: Professor Gerald G. Mace, Department of Atmospheric Science, University of Utah, 135 S 1460 E, Rm. 819 (WBB), Salt Lake City, UT 84112-0110.
E-mail: jay.mace@utah.edu

DOI: 10.1175/JAMC-D-12-0102.1

© 2013 American Meteorological Society

leads to minimal feedback variability attributable to high clouds. This consistent change in forcing among the models is apparently due to a robust dynamical response of changes to anvil temperature driven by a mechanism proposed by Zelinka and Hartmann (2010).

These findings suggest a couple of possibilities, the most intriguing of which could be that GCM parameterizations of high clouds are now sufficiently accurate to represent these clouds within a changing climate. It could also be that the feedbacks are consistently wrong in terms of either magnitude or mechanism across the ensemble. This possibility remains to be determined. A third possibility, discussed by Stephens (2005), is that the climate sensitivity and cloud feedback as defined are not capable of revealing fundamental deficiencies in the model simulations.

Pincus et al. (2008) find no correlation between cloud feedbacks and the skill of the AR4 models to simulate clouds and precipitation. Consistent with this finding, the ice water path (IWP) has been shown to vary by more than a factor of 6 among these models (Waliser et al. 2009). One could reasonably question what the implications for the simulated climates must be for this range of variability in such a fundamental parameter. This disconnect between skill to represent the physical state of the climate and the feedbacks to the climate system is likely a result of the relatively simple method that is employed now by the modeling community to define cloud feedback. This quantity cannot capture the consequences of large intermodel variability in high-cloud properties as long as the change in radiative forcing due to high-cloud changes is consistent. This contention is borne out by the results of Williams and Webb (2009) who compared cloud radiative forcing for various objectively defined cloud regimes with retrieved cloud properties that used Moderate Resolution Imaging Spectroradiometer (MODIS) and International Satellite Cloud Climatology Project (ISCCP) satellite data. They find definite biases in longwave cloud forcing for tropical and midlatitude cirrus that suggest the models are producing high clouds that are generally too thick (i.e., have too strong of a longwave cloud forcing) relative to measurements. This high bias in longwave cloud forcing suggests that the model climates are using cirrus to offset other significant problems in the simulated hydrological cycle that must have consequences elsewhere.

Stephens (2005), who presents a critical discussion of the current feedback diagnostic method, suggests that the basis for understanding feedbacks in general and cloud feedbacks in particular lies in developing a clearer understanding of the relationships between large-scale circulation regimes and the cloud systems that populate them. Williams and Webb (2009), Williams and Tselioudis (2007), and Jakob (2003) give examples of this approach that use ISCCP radiative cloud properties. Several studies have examined the relationship between cirrus clouds and the large-scale environment (Heymsfield 1977; Starr and Wylie 1990; Mace et al. 1995, 2006a; Sassen and Campbell 2001). Most of these studies have focused on data from field campaigns or ground-based remote sensing data from a single location. In this study we take advantage of information from the A-Train (Stephens et al. 2002) to study the vertical structure of cirrus on a large spatial scale during a full annual cycle.

Our objectives are to determine to what extent and in what manner the large-scale dynamics and cirrus cloud properties are coupled. The essence of our approach is to ask, Given objective classifications of cirrus vertical structure, to what extent are the large-scale dynamics uniquely determined? A similar but converse question that we also address is, Given objective classifications of large-scale dynamics regimes that tend to produce cirrus, are the cirrus properties uniquely determined? The answers to these questions have implications for the degree of detail required in and the complexity of cirrus parameterizations in large-scale models. If cirrus properties are uniquely determined by their large-scale environments, then the essence of cirrus effects on the climate will be accurately characterized with reasonably simple parameterizations. A more complicated answer to these questions, on the other hand, would imply that cirrus must be treated in a manner that allows for realistic subgrid-scale variability so as to capture their radiative effects and ultimately their feedbacks.

The rest of the manuscript is organized as follows: Section 2 describes the data and analysis techniques used to define and characterize cirrus. Section 3 details the cirrus types that were identified from a classification algorithm that is based on vertical structure or that is based on large-scale dynamics. Section 4 presents a summary of the findings from this study.

2. Method

Since our objectives are to examine cloud fields that have significant vertical structure, substantial temporal and spatial variability, and possible coupling to the meteorological environment, we use a combination of A-Train measurements, geostationary satellite data, and meteorological reanalyses. The A-Train is a constellation of polar-orbiting Earth-observing satellites (Stephens et al. 2008). The flagship A-Train satellite (*Aqua*) was launched in 2002 (Parkinson 2003) and carries passive radiometric instruments that image Earth in a number of spectral bands that range from the ultraviolet

to microwave. The A-Train was augmented in mid-2006 with the active remote sensing satellites *CloudSat* and *Cloud–Aerosol Lidar and Infrared Pathfinder Satellite Observations* (*CALIPSO*), which carry, respectively, the Cloud Profiling Radar (CPR; Im et al. 2006) and the Cloud–Aerosol Lidar with Orthogonal Polarization (CALIOP; Winker et al. 2007). The CPR and CALIOP footprints were collocated in space and were only a few tens of seconds apart in time during the period of this study.

TABLE 1. Bulk statistical properties of the all-cirrus events identified in the *CloudSat–CALIPSO* dataset over the Atlantic basin during 2007. Shown are the mean, the standard deviation, and the median in parentheses of the distribution of the quantity.

Top (km)	12.6 ± 2.4 (12.6)
Base (km)	9.3 ± 3.2 (9.4)
Thickness (km)	3.3 ± 2.2 (2.7)
Top temperature (°C)	−62.5 ± 11.5 (−62.2)
Base temperature (°C)	−38.9 ± 18.7 (−38.7)
Max (dBZ) temperature (°C)	−46.7 ± 17.2 (−46.6)
Ice water path (g m^{-2})	83.0 ± 186.3 (17.5)

a. Cirrus occurrence and microphysics

Cloud microphysical and radiative properties and profiles of radiometric fluxes for all hydrometeor layers along the *CloudSat* track are derived using a suite of techniques that are described in Mace (2010; hereinafter M10). We use the MODIS visible optical depths from the MODIS Level 2 Joint Atmosphere Product (Platnick et al. 2003) as well as solar and IR fluxes derived from Clouds and the Earth's Radiant Energy System (CERES; Wielicki et al. 1998) and liquid water paths derived from Advanced Microwave Scanning Radiometer for Earth Observing System (AMSR-E) microwave brightness temperatures (Wentz and Meissner 2000) in the retrieval of liquid- and ice-cloud properties. The method that we apply is adapted from techniques that we first applied to a similar ground-based dataset (Mace et al. 2006b, 2008). To this suite of algorithms we implement additional schemes designed specifically for the A-Train data (Zhang and Mace 2006c; appendix A of M10). The algorithm suite is embedded within an iterative scheme that attempts to minimize the differences with CERES fluxes by adjusting empirical parameters within the retrieval algorithms. Using comparisons with in situ data and comparisons with other cloud-property retrieval algorithm results (*Aqua*–MODIS cloud product, AMSR-E liquid water path product, and the radar-only *CloudSat* cloud water content product), M10 shows that uncertainty in ice water content (IWC) and LWC is on the order of 70% and 50%, respectively, and that characteristic errors in IWP and LWP would be on the order of 40% if random, uncorrelated, and unbiased error statistics are assumed. These assumptions, of course, imply that these error estimates are lower bounds on the actual errors.

Because we are focusing on a specific cloud type in the upper troposphere where ice-phase processes are predominant (cirrus), it is necessary that we establish a reasonably objective set of criteria that identifies where cirrus layers are a significant feature of the cloud distribution. The *CloudSat* products known as Geometrical Profiling Product (GEOPROF)-lidar (Mace et al. 2009) and the European Centre for Medium-Range Weather Forecasts (ECMWF) Auxiliary product (Partain 2004) are used to identify cirrus events by using a method adapted from Mace et al. (2006a). The GEOPROF-lidar product provides a radar–lidar cloud mask, which identifies the location of cloud layers in the vertical direction. The ECMWF Auxiliary product provides ECMWF state variable data that have been interpolated to each radar bin. Cirrus are taken to be vertically isolated, ice-phase hydrometeor layers in the upper troposphere. In general, for a hydrometeor layer to be defined as cirrus, we require the cloud-top temperature to be colder than −30°C, the temperature of the layer-maximum radar reflectivity to be colder than 0°C, and the cloud-base temperature to be colder than 0°C. For our purposes, we then define cirrus events as 100 consecutive profiles (approximately 180 km in length) from a *CloudSat* orbit with at least 75% of the profiles containing cirrus layers. The event length used here is somewhat arbitrary, but the length is approximately one-fifth of the typical synoptic length scale, and our results are not sensitive to this decision. Focusing on the Atlantic Ocean basin region from 60°S to 60°N latitude and from −15° to −60° longitude during the calendar year of 2007, since this is where we have geostationary satellite data, we identify a total of 32 527 cirrus events in the merged *CloudSat* and *CALIPSO* data. This number equates to 3 252 700 *CloudSat* footprints or, if one assumes that the along-track length of the *CloudSat* footprint is 1.8 km, 6×10^6 linear kilometers of cirrus.

Table 1 summarizes the basic physical statistics of the cirrus layers that we identify. Cirrus cloud bases have a mean value and standard deviation of 9.3 ± 3.2 km, and cirrus cloud tops have a mean value and standard deviation of 12.6 ± 2.4 km. For comparison, Sassen et al. (2008, hereinafter S08) described the global distribution of cirrus clouds from a similar A-Train climatological database. S08 found that the global average cirrus thickness was 2 km, with cirrus bases (tops) ranging from about 7 km (8 km) in the high latitudes, to near 12.5 km (15 km) in the tropics. While our range of values for cirrus cloud base and top agrees well with S08,

our average cirrus cloud thickness was slightly larger (3.3 ± 2.2 km), with a median value of 2.7 km. Our cirrus-top temperatures have a mean value and standard deviation of −62.5 ± 11.5°C, and base temperatures have a mean value and standard deviation of −38.9 ± 18.7°C. These results reveal that most cirrus events easily exceed the threshold to be considered cirrus (base temperature of <0°C and top temperature of <−30°C). S08 found that cirrus cloud-base temperatures ranged from about −40° to −55°C and cirrus-top temperatures ranged from approximately −60° to −70°C. Our cirrus-base temperatures are considerably warmer than those found by S08. These differences in cirrus thickness and base temperature can be attributed to different definitions of cirrus, primarily that S08 has a more stringent optical thickness definition that requires that the CALIOP beam not be fully attenuated when traversing the layer. S08 base their cirrus definition on the visual impact of the cloud to a surface observer and therefore restrict cirrus to having a visible optical depth of less than approximately 4. Our cirrus definition is based on identifying clouds in the upper troposphere that are primarily composed of ice and are derived from ice-phase processes, and therefore we impose no such optical thickness restriction here, which means that we will identify more thick cirrus than did S08.

b. *Cluster analysis of cirrus events*

The National Centers for Environmental Prediction–National Center for Atmospheric Research (NCEP–NCAR) reanalysis data (Kalnay et al. 1996; Kistler et al. 2001) are used in this study to place the cirrus events in large-scale meteorological contexts. The reanalysis data contain dynamic and thermodynamic variables on a 2.5° latitude–longitude grid and 17 vertical levels. These variables are available four times per day at 0000, 0600, 1200, and 1800 UTC. In this study, we examine the geopotential height, horizontal and vertical wind, absolute vorticity, and relative humidity (RH) at various pressure levels. While the temporal and spatial scales of the reanalysis are coarse, the reanalysis is sufficient to describe the overall large-scale setting. We examine the large-scale meteorological situation by creating composites of the dynamics in 40° × 60° latitude–longitude regions centered on individual cirrus events and by objectively classifying the dynamical state of regions containing cirrus, as described next.

The set of questions that we wish to explore pertains to the relationships that exist between cirrus properties (bulk and microphysical) that can be derived from A-Train data and the large-scale environments in which the cirrus are found. To address these questions we use the vertical structure of cirrus layers defined by patterns of radar reflectivity as a function of pressure to objectively identify cirrus types on the basis of their morphological structure. Our objective here is to determine whether cirrus events actually separate into distinct populations determined by vertical structure and whether we can identify relationships between the large-scale dynamics and these morphological types. In a second independent classification approach we take regions containing cirrus and identify meteorological states on the basis of large-scale dynamics. We then examine to what extent cirrus properties depend on these dynamical states.

To accomplish these goals a *K*-means clustering algorithm (Anderberg 1973) is used. The *K*-means technique is a nonhierarchical classification algorithm that allows for the reassignment of observations as the analysis progresses. The *K*-means method is named for the number of clusters *K* into which the data are grouped. Several studies have used the *K*-means algorithm to classify clouds on the basis of the ISCCP cloud-top pressure and optical-depth retrievals (Jakob et al. 2005; Rossow et al. 2005; Gordon and Norris 2010). After the cloud clusters are defined, the dynamics associated with these cloud scenes can be investigated to gain an understanding of how the dynamics is related to the cloud structures. (Gordon et al. 2005; Jakob et al. 2005). This approach has been applied more recently to *CloudSat* data using radar reflectivity *Z* and pressure *P* joint histograms (Zhang et al. 2007).

In our implementation of the approach used by Zhang et al. (2007), joint histograms of *P–Z* are developed for each 100-profile cirrus event from January to December of 2007 over the Atlantic basin. These histograms consist of seven pressure bins (ranging from 1000 to 50 hPa) and seven *Z* bins (ranging from −32 to +30 dB*Z*) as in Fig. 1b. The histograms contain all clouds that are present within a cirrus event, including lower-level clouds. For each cirrus event we create a *P–Z* histogram by classifying each cloudy radar observation into its respective pressure and *Z* bin. Then we divide the *P–Z* histogram by the total number of cloudy radar observations, so that the total relative frequency of occurrence sums up to 100% for each cirrus event. Cirrus that were detected only by the lidar are given a nominal radar reflectivity (=−32 dB*Z*) just below the −30-dB*Z* minimum detection threshold of the *CloudSat* CPR (Stephens et al. 2008) for this analysis. This means that the smallest *Z* bin (<−30 dB*Z*) represents the lidar-only portion of cirrus. The *K*-means algorithm is then applied to the *P–Z* histograms for each cirrus event observed over the Atlantic basin in 2007. The only restriction on the initial seeds to the *K*-means algorithms is that the correlation between them must be less than 0.7 to ensure that the initial seeds are not too closely related.

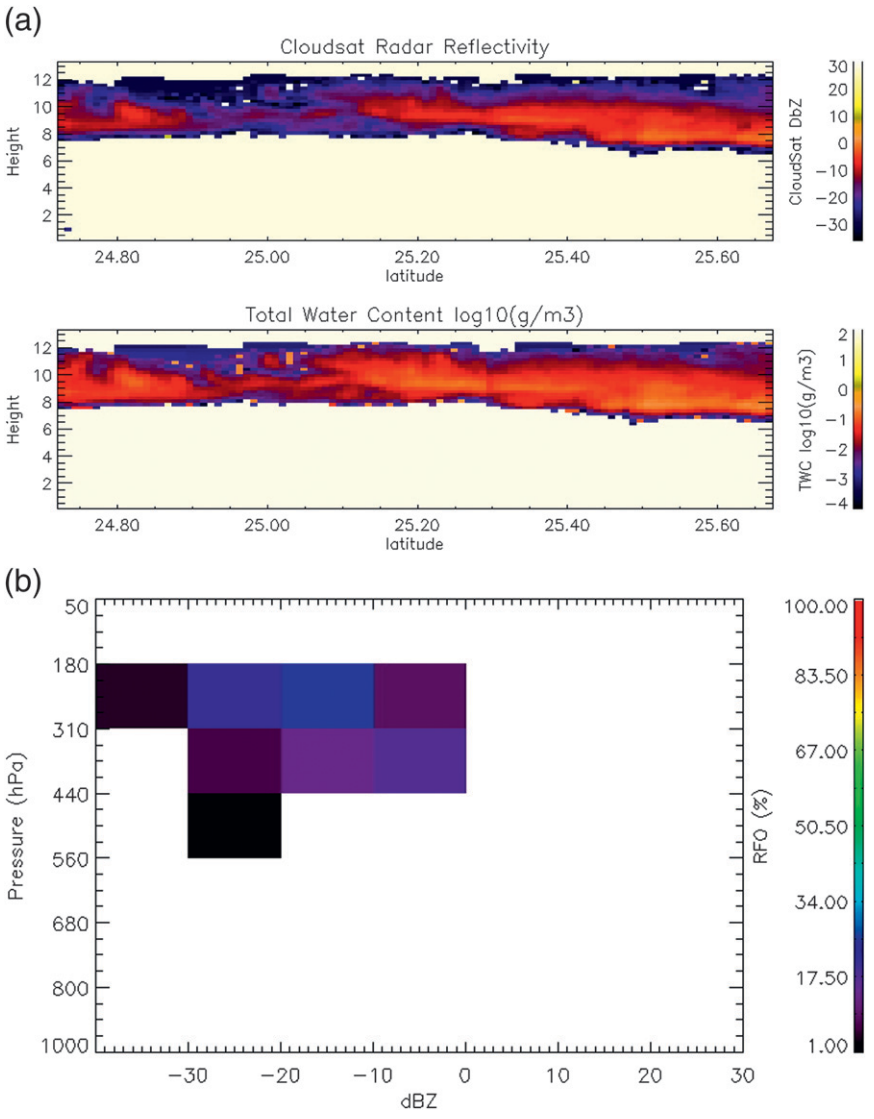

FIG. 1. An example cirrus event at 25°N, 37.5°W from *CloudSat* orbit 4067 on 1 Feb 2007 at approximately 1554 UTC: (a) the *CloudSat* radar reflectivity and derived ice water content and (b) the *P–Z* histogram for this case study. The RFO of each *P–Z* pair is shown in the color bar. Values of Z that are less than −30 dBZ (leftmost bin of histogram) correspond to cirrus observed only by the lidar.

In this study, each cirrus event is assigned to a cluster whose vector-mean set of properties that describe the event has the minimum distance from a cluster centroid. The distance measure we use in this analysis is a weighted Euclidean distance d, defined in Wilks (2006) as

$$d_{i,j} = \left[\sum_{k=1}^{K} w_k (x_{i,k} - x_{j,k})^2 \right]^{1/2}. \qquad (1)$$

The Euclidean distance in the K-dimensional space is used to measure the distance between two vectors: $\mathbf{x}_i$, which is the vector for the cluster centroid, and $\mathbf{x}_j$, which is the vector for the individual cirrus event that is being classified. For clustering that is based on patterns of *P–Z*, the weights w_k are equal to 1 for each k (i.e., each *P–Z* bin in the histogram) since the units [relative frequency of occurrence (RFO; %)] are the same, which means that the distance equation reduces to the ordinary Euclidean distance.

The cluster centroid is recalculated each time that an element is assigned to the cluster. The algorithm continues to iterate until a full cycle through the data leads to no reassignments. For this study, 10 iterations were

sufficient for the algorithm to converge. Because the results depend on the initial seeds, the cluster analysis was run several times to arrive at a consensus result. Determining how many clusters are sufficient to reasonably characterize the variability in cirrus properties or the large-scale meteorological environment is subjective. The ultimate goal of the cluster analysis is to maximize the similarity within each cluster, while simultaneously minimizing the similarity between clusters. We follow the method from Rossow et al. (2005) and use the following criteria to judge the outcome of the analysis: 1) the resulting centroid histogram patterns must not change greatly for different initial seeds, 2) the resulting centroid patterns should differ from each other substantially (pattern correlation should be less than 0.8), and 3) the distance between cluster centroids should be larger than the dispersions of the cluster-member distances from the centroid. We define the final set of clusters as a set of regimes, henceforth.

In addition to the *P–Z* regimes, we also create dynamics regimes that are independent of the *P–Z* classifications for which the only prerequisite is that a cirrus event is diagnosed using the *CloudSat–CALIPSO* data along the *CloudSat* track. Classifying cirrus cloud systems on the basis of the large-scale dynamical environment in which the cloud systems are evolving provides information on whether cirrus properties vary systematically across the dynamics continuum. Sassen and Campbell (2001) found that cirrus clouds are often observed in many different synoptic situations. Using the A-Train-derived cirrus events, we select the data point in the reanalysis that is closest in space and time to the cirrus event. The dynamics are classified in a manner similar to the creation of the *P–Z* regimes, with the *K*-means algorithm using five large-scale dynamical parameters that are derived from the NCEP–NCAR reanalysis data. The parameters are not independent of each other, but they are diagnostically related to the synoptic-scale weather regimes that tend to generate large-scale upper-tropospheric cloudiness. The quantities are 300-hPa relative humidity, 300-hPa pressure velocity, 500-hPa pressure velocity, 500-hPa absolute vorticity advection, and 850-hPa temperature advection. The large-scale dynamics quantities are calculated for each of the 32 527 cirrus events, and the standardized vectors are used in the clustering algorithm.

The weights used for the dynamics clustering [Eq. (1)] are the reciprocals of the corresponding variances s^2 of the quantities: $w_k = 1/s^2$. The resulting function of the standardized variables is called the Karl Pearson distance. The Karl Pearson distance is used for the dynamic clustering because the dynamic variables have inconsistent measurement units.

Because the cluster analysis algorithm is applied to a large region (from 60°N to 60°S), it is important to be aware of how some of the dynamical values are inherently related to latitude. For example, temperature advection and absolute vorticity are expected to be greater in the extratropics than in the tropics. To account for the sign difference in vorticity between the hemispheres, the Northern Hemisphere sign convention is used throughout, and values of absolute vorticity advection in the Southern Hemisphere are multiplied by −1 for the clustering analysis.

To quantify the most reasonable number of dynamics regimes we examined the average Karl Pearson distances between the individual cirrus events and their corresponding cluster centroids, as well as the Karl Pearson distance between the cluster centroids. The goal of the cluster analysis is to minimize the within-cluster distance (essentially the difference between the cluster centroid and individual cirrus events belonging to the cluster) while simultaneously maximizing the distance between the clusters. This ensures that the resulting regimes are unique and that the cirrus events within a regime are similar.

c. Lagrangian tracking of cirrus events

Since the A-Train measurements provide only an instantaneous snapshot of a cirrus event, geostationary satellite data are used to study the cloud-field tendencies. The cloud fields measured by A-Train are tracked forward and backward in time by using a geospatial coherence algorithm (Soden 1998). The geostationary satellite data used in this study were observed by the Spinning Enhanced Visible and Infrared Imager (SEVIRI) imaging radiometer on the Meteosat Second Generation satellites (Schmetz et al. 2002). Cirrus evolution is studied with Lagrangian trajectories in which water vapor channel radiance patterns are followed in time with sequential satellite images (Soden 1998; Mace et al. 2006c).

Cirrus events are tracked using half-hourly observations from 6.2-μm brightness temperatures derived from SEVIRI data. The tracking algorithm is adapted from the algorithm described in Mace et al. (2006c). An initial reference box of 100 km × 100 km that describes the radiance pattern is centered on a cirrus event that was observed from the *CloudSat–CALIPSO* data. The size of the search area is a 280 km × 280 km box centered on the cirrus event. The extent of the search area was determined by calculating the maximum distance the cloud could move from one image to the next, based on a 50 m s^{-1} wind over a 30-min period. The algorithm searches for the highest spatial correlation between the original radiance pattern and all possible matches at the

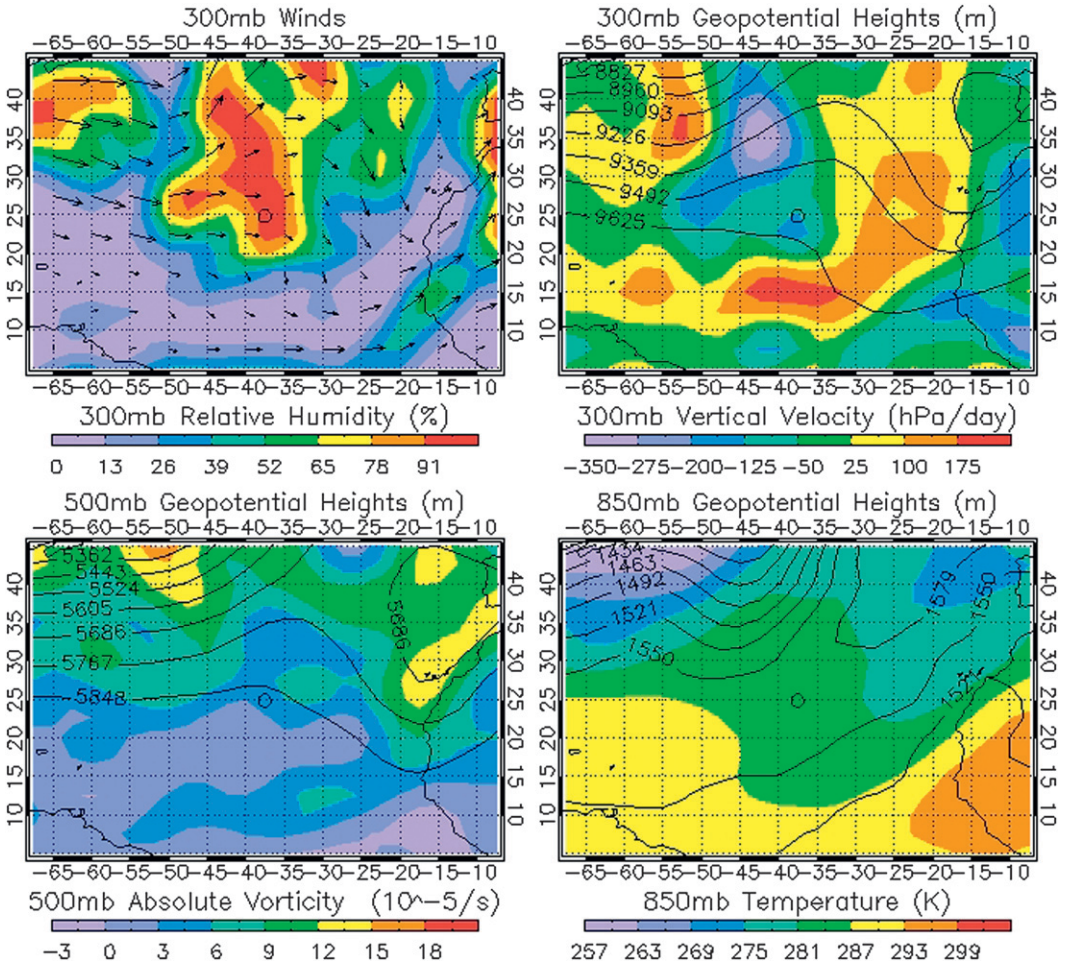

FIG. 2. Large-scale dynamics derived from the NCEP–NCAR reanalysis at 1800 UTC 1 Feb 2007 surrounding the cirrus case study shown in Fig. 1. The *y* axis is latitude, and the *x* axis is longitude. The location (+25°, −37.5°) of the cirrus event is denoted by the open circle. The quantities that are contoured are shown in the titles above each panel, and the quantities depicted in color are given in the labeled color bars below each panel.

next and previous time step by replicating 100 km × 100 km boxes and performing a 1:1 correlation between pixels in the original and the candidate boxes. The box in the search area that has the highest correlation with the reference box is designated as the destination box. The destination box then becomes the reference box, and the process is repeated. We apply the tracking algorithm to radiance patterns from successive water vapor images backward in time for approximately 3 h and then forward in time for approximately 3 h, for a total of 6 h of tracking centered on the A-Train passage over the event.

In general, if the 100 km × 100 km box-average 6.2-μm brightness temperature Tb of the cirrus event is observed to be increasing (decreasing) in time, the cirrus event is considered to be dissipating (deepening). Changes in the 6.2-μm brightness temperature are due to changes in the cirrus microphysics that modify the broadband emission, among other things. Therefore, if Tb is changing over time, we assume that the amount and/or temperature of the ice condensate is changing, and we interpret it to mean that the cloud is either growing (deepening) or dissipating (thinning).

The definition that we use to classify a cirrus event as deepening or dissipating involves several criteria relating to how the average Tb changed in time. To determine the strength and consistency of the cirrus cloud evolution, several factors are considered. The correlation of Tb with time for the whole tracking period, the rate of change of Tb with time, and the difference in the mean temperature before and after the *CloudSat* overpass ($\Delta Tb = Tb_{after} - Tb_{before}$) are determined. For an event to be classified as dissipating, the evolution of the Tb with time must have a moderate correlation coefficient ($r \geq 0.3$), measureable slope [$m \geq 0.1$ K (0.5 h)$^{-1}$], and

a noticeable change in the average Tb from before and after the *CloudSat* overpass ($\Delta T \geq 0.5$ K). The same criteria are used for growing events, except the sign of the correlation coefficient, slope, and change in Tb is required to be negative ($r \leq -0.3$, $m \leq -0.1$ K $(0.5\ \text{h})^{-1}$, and $\Delta T \leq -0.5$ K). Cirrus events that failed to meet the definition for growing or dissipating did not have consistency in their Tb evolution or exhibited little change in their average Tb with time. These cirrus events were classified as undetermined (22.7% of all cases) as to their evolution.

3. Results

An example cirrus event to which we will return as an illustration of the analysis method is presented in Fig. 1. This cirrus event was observed near +25° latitude, −37.5° longitude on 1 February 2007 from *CloudSat* orbit 4067. The cirrus-layer base is found to have been located between 6 and 8 km, and the layer top was near 12 km. The maximum reflectivity (-1 dBZ_e) was located near cloud base close to the northern boundary of the event. This cirrus layer had a mean thickness of approximately 4 km, which is thicker than the average cirrus layer but still within 1 standard deviation of the mean thickness. The mean IWP for the cirrus event in Fig. 1 is estimated to have been 164 g m^{-2}. This value of IWP is larger by about a factor of 2 than the overall mean IWP given in Table 1, but, given the skewed distribution of IWP, the retrieved value is not atypical. Figure 2 displays the NCEP–NCAR data for this case study. At 500 hPa, the cirrus event was associated with weak anticyclonic vorticity advection due to a ridge at upper levels. Negligible temperature advection is noted at 850 hPa, owing to nearly calm winds and weak temperature gradients in the vicinity of a lower-tropospheric high pressure region. From satellite imagery (Fig. 3a) the case study was associated with a band of cirrus that formed downstream of a frontal cloud shield. The dynamics associated with the front are evident in Fig. 2 to the northwest of the cirrus event. The high-level cloud layer sampled by the A-Train in this large-scale regime existed in the anticyclonic region of the trough–ridge system primarily from the upstream inflection point of the flow to and just downstream of the ridge axis. The synoptic situation for this cirrus event shown in Fig. 2 is similar to the ''ridge axis'' cloud band that was described by Starr and Wylie (1990), given that the cirrus was situated along the ridge axis and in a region of ascent at 300 hPa. The event considered here was located just upstream from the axis of the 300-hPa ridge in a region of maximum relative humidity. This region was situated in the exit region of a curved jet that was rounding the base of the upstream trough. Such

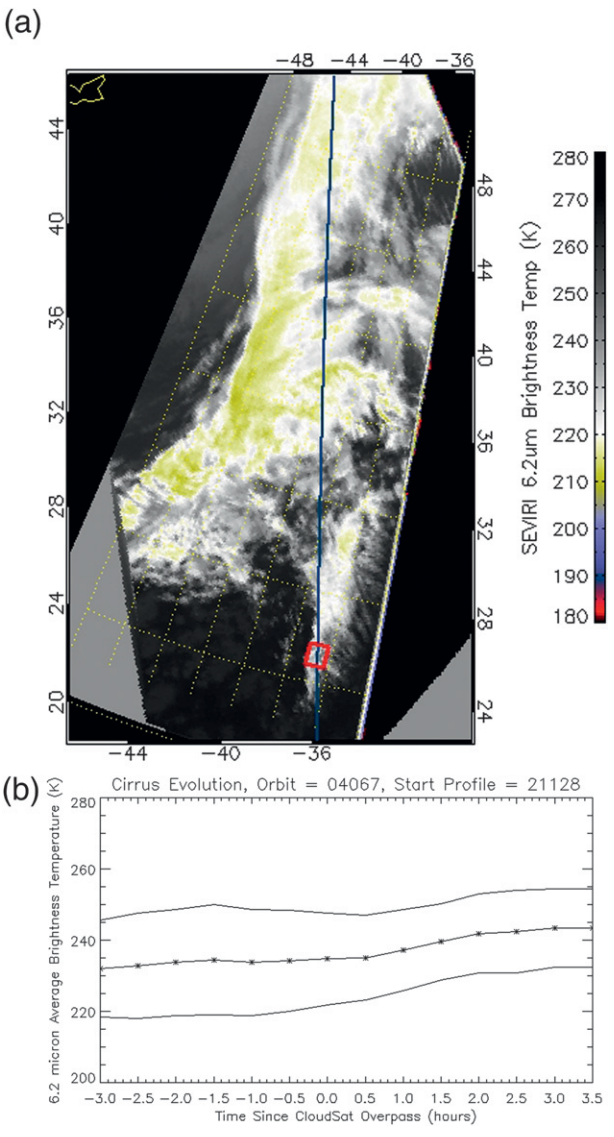

FIG. 3. (a) 6.2-μm imagery for the case study observed by the SEVIRI geostationary imager at 1600 UTC 1 Feb 2007. The blue line is the *CloudSat* orbit, and the red box denotes the location of the cirrus event in Figs. 1 and 2. The radiances are converted to brightness temperatures, as shown in the color bar, for display. (b) The trend in brightness temperature at 6.2 μm during the hours prior to and after the *CloudSat* overpass. The solid lines show the standard deviation.

regions are known to be centers of upper-tropospheric divergence (Shapiro and Kennedy 1981; Mace et al. 1995). The large-scale ascent (3.2 cm s^{-1} at 300 hPa) that was associated with the ageostrophic indirect circulation in this region (Fig. 2) likely maintained the upper-tropospheric relative humidity maximum in which the cirrus were observed (Fig. 3a).

By tracking the cloud system through time from 3 h prior to the overpass until 3 h after (Fig. 3b), we find that

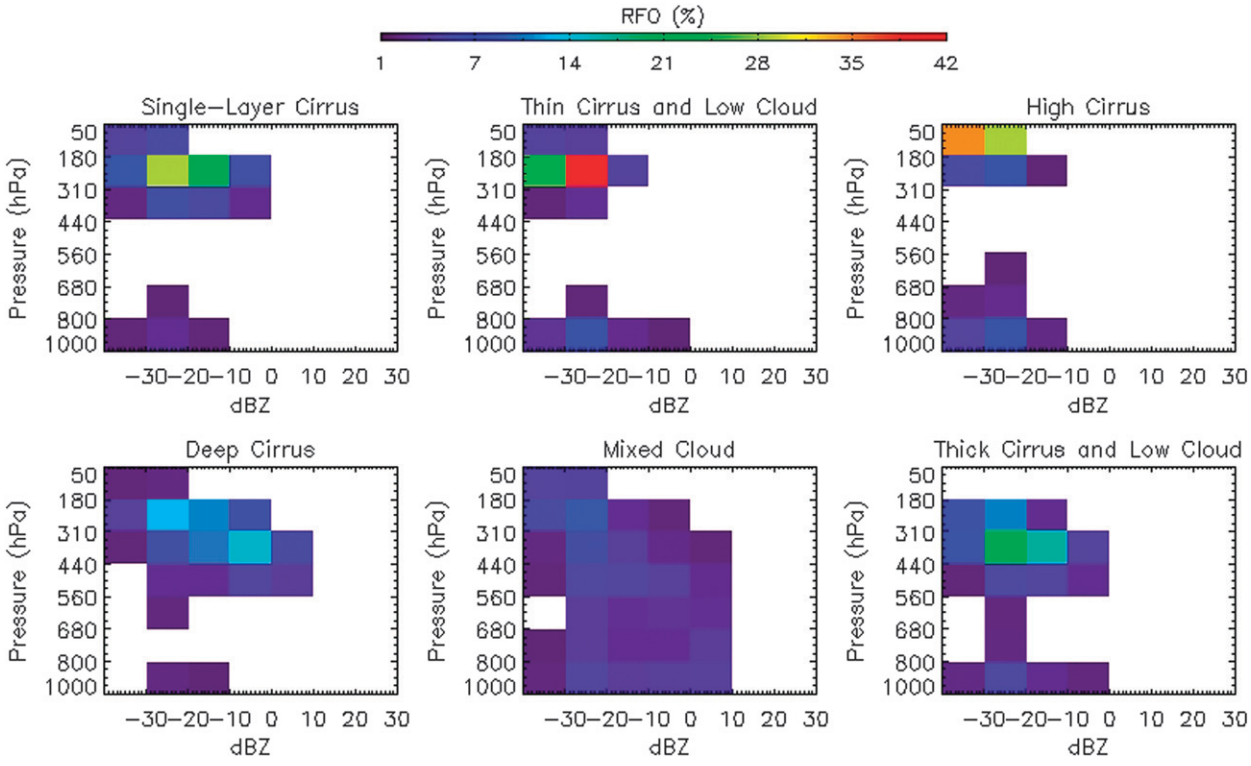

FIG. 4. The *P–Z* histograms of the six *P–Z* regimes. For each histogram, the sum of the relative frequencies is equal to 100%. The descriptive names used in the text are shown in the title of each panel. Values of Z that are less than −30 dBZ (leftmost bin of histogram) correspond to cirrus observed only by the lidar.

the Tb of this cirrus event gradually warmed. The change in Tb with time has a correlation coefficient of $r = 0.95$, a slope of $m = 0.95$ K (0.5 h)$^{-1}$ and $\Delta T = 6.9$ K, and therefore this cirrus event is classified as dissipating. Three hours before the *CloudSat* overpass the average Tb of the cirrus event in the 6.2-μm channel was 232 K, and 3.5 h after the *CloudSat* overpass the cirrus event had warmed to 243 K, which is an overall increase of 11 K in 6.5 h.

a. Cirrus regimes defined by P–Z morphology

The six *P–Z* regimes that were determined to be significant from the data collected in the Atlantic basin during 2007 are shown in Fig. 4, and their bulk physical properties are summarized in Table 2. The geographic distributions of these layer types are shown in Fig. 5, and Figs. 6 and 7 illustrate the distribution of IWC and the composite large-scale dynamics of the *P–Z* regimes, respectively. Table 3 summarizes the large-scale dynamical quantities of the *P–Z* regimes. From the characteristics of the *P–Z* histograms, we assign descriptive names to the regimes for ease of discussion.

The case study shown in Figs. 1–3 falls into the single-layer cirrus regime on the basis of its vertical distribution of radar reflectivity. The Euclidian distance of this case from this *P–Z* centroid is within 1 standard deviation of the mean distance for single-layer cirrus. A comparison of Fig. 1b with Fig. 4 shows that the event appears visually to be most closely associated with either single-layer cirrus or deep cirrus, although the event did not have any radar reflectivity measurements in excess of 0 dBZ as are found in the deep cirrus regime. In terms of its properties, we find that the event is within 1 standard deviation of all bulk properties for this *P–Z* regime except IWP (Table 2). With an IWP of 164 g m^{-2}, this case is more than 2 standard deviations greater than the average single-layer cirrus case. Consistent with this result, the large-scale vertical motion is +3.2 cm s^{-1} for this case, whereas the average large-scale ascent for single-layer cirrus is +0.93 cm s^{-1} (Table 3). The more strongly positive large-scale ascent is associated with relative humidity at 300 hPa that is approximately 90%, whereas the average single-layer cirrus case is 44%.

A first glance at Fig. 4 suggests that the *P–Z* composites are strongly related to one another with only subtle differences between them. To gauge the similarity of the *P–Z* clusters, we calculated the pattern correlation between the different cloud (*P–Z*) patterns shown in Fig. 4. The pattern correlation is the correlation of the *P–Z* cluster histograms, which are expressed as

TABLE 2. Bulk properties of the *P–Z* regimes. Cell contents are as in Table 1.

	Single layer	Thin cirrus/low cloud	High cirrus	Deep cirrus	Mixed cloud	Thick cirrus/low cloud
No. of events and RFO	5271 (16%)	5713 (18%)	5896 (18%)	4969 (15%)	6880 (21%)	3798 (12%)
Top (km)	12.9 ± 1.5 (12.7)	12.3 ± 1.1 (12.3)	15.4 ± 1.0 (15.3)	11.8 ± 1.8 (11.6)	12.3 ± 3.0 (12.6)	9.9 ± 1.7 (9.7)
Base (km)	9.4 ± 1.3 (9.3)	10.3 ± 1.1 (10.4)	13.3 ± 1.4 (13.3)	6.3 ± 1.8 (6.4)	8.7 ± 3.8 (9.2)	6.7 ± 1.7 (6.8)
Thickness (km)	3.4 ± 1.6 (3.2)	1.9 ± 1.1 (1.8)	2.0 ± 1.4 (1.6)	5.5 ± 1.9 (5.5)	3.6 ± 2.5 (2.9)	3.2 ± 1.8 (2.8)
Top temperature (°C)	−61.8 ± 9.0 (−61.4)	−60.8 ± 6.3 (−61.3)	−75.0 ± 5.14 (−76.4)	−58.0 ± 9.6 (−57.7)	−62.4 ± 12.6 (−62.6)	−51.5 ± 9.3 (−51.2)
Base temperature (°C)	−35.2 ± 8.7 (−35.3)	−46.3 ± 8.0 (−46.5)	−62.8 ± 10.3 (−63.3)	−17.8 ± 9.1 (−17.1)	−36.8 ± 19.9 (−38.0)	−28.0 ± 10.3 (−27.9)
Max (dBZ) temperature (°C)	−44.0 ± 7.8 (−43.9)	−52.8 ± 6.7 (−53.3)	−69.5 ± 7.8 (−69.9)	−27.7 ± 8.8 (−27.2)	−44.5 ± 18.4 (−45.9)	−35.4 ± 9.2 (−35.1)
Ice water path (g m^{-2})	47.8 ± 53.1 (35.6)	7.9 ± 7.9 (5.5)	5.3 ± 15.1 (2.73)	262.8 ± 255.0 (180.5)	140.7 ± 282.7 (22.7)	42.8 ± 45.7 (29.7)

two-dimensional (pressure and *Z*) vectors of RFO. The two clusters that are the most highly correlated are single-layer cirrus and thin cirrus with low cloud, which have a pattern correlation coefficient of 0.78. In a similar way, deep cirrus and thick cirrus with low cloud are also strongly correlated. A closer look at the bulk properties and the large-scale dynamics of these regimes reveals significant differences between these correlated types, however. Most obvious, perhaps, are the differences in layer-average properties. For instance, single-layer cirrus and thin cirrus with low cloud, while strongly correlated in their *P–Z* structures, are very different in their mean IWPs: 48 and 8 g m^{-2}, respectively (Table 2). This contrast in IWP occurs because of a tendency toward more IWC in the middle one-third of the single-layer cirrus cases (Fig. 6). We also find that this difference in IWP appears to be strongly related to the intensities of the composite large-scale dynamics of these types. Single-layer cirrus, for instance, has a mean vertical ascent at 300 hPa of +0.93 cm s^{-1}, whereas this quantity is weaker for thin cirrus with low cloud for which the large-scale ascent at 300 hPa is effectively zero (Table 3). Of interest, however, is that the large-scale synoptic pattern (Fig. 7) is much better defined for the thin cirrus with low cloud, where the layers often tend to be situated near the exit region of a 300-hPa jet streak and in the gradient between ascent and descent at 500 hPa. The geographic distributions of these two types, shown in Fig. 5, also helps to differentiate them, with single-layer cirrus occurring most frequently in the tropics and subtropics and thin cirrus with low cloud being more likely to be found in the Northern Hemisphere midlatitudes.

The other two strongly correlated types, deep cirrus and thick cirrus with low cloud, are also mostly evenly distributed throughout the study domain, but they also reveal very substantial differences in their physical and dynamical properties. The IWP of deep cirrus is in excess of 260 g m^{-2} (Table 2) and exists in a large-scale dynamical environment that is strongly ascending at +2.05 cm s^{-1} at 300 hPa (Table 3). The motion of the thick cirrus with low cloud is substantially weaker, although still ascending at +0.58 cm s^{-1} at the 300-hPa level. The mean IWP of thick cirrus with low cloud is accordingly also much less, at 43 g m^{-2}. The differences in IWP are due both to a generally greater cloud-layer depth for the deep cirrus type and also to the presence of larger IWC values. The deep cirrus type typically has peak IWC values in the middle portion of the layer that are in excess of 0.1 g m^{-3}, whereas thick cirrus with low cloud attains peak values that are about a factor of 10 less on average, as shown in Fig. 6. The deep cirrus is associated with a peak in ascent that is nearly centered on the point of measurement, whereas the thick cirrus with low cloud

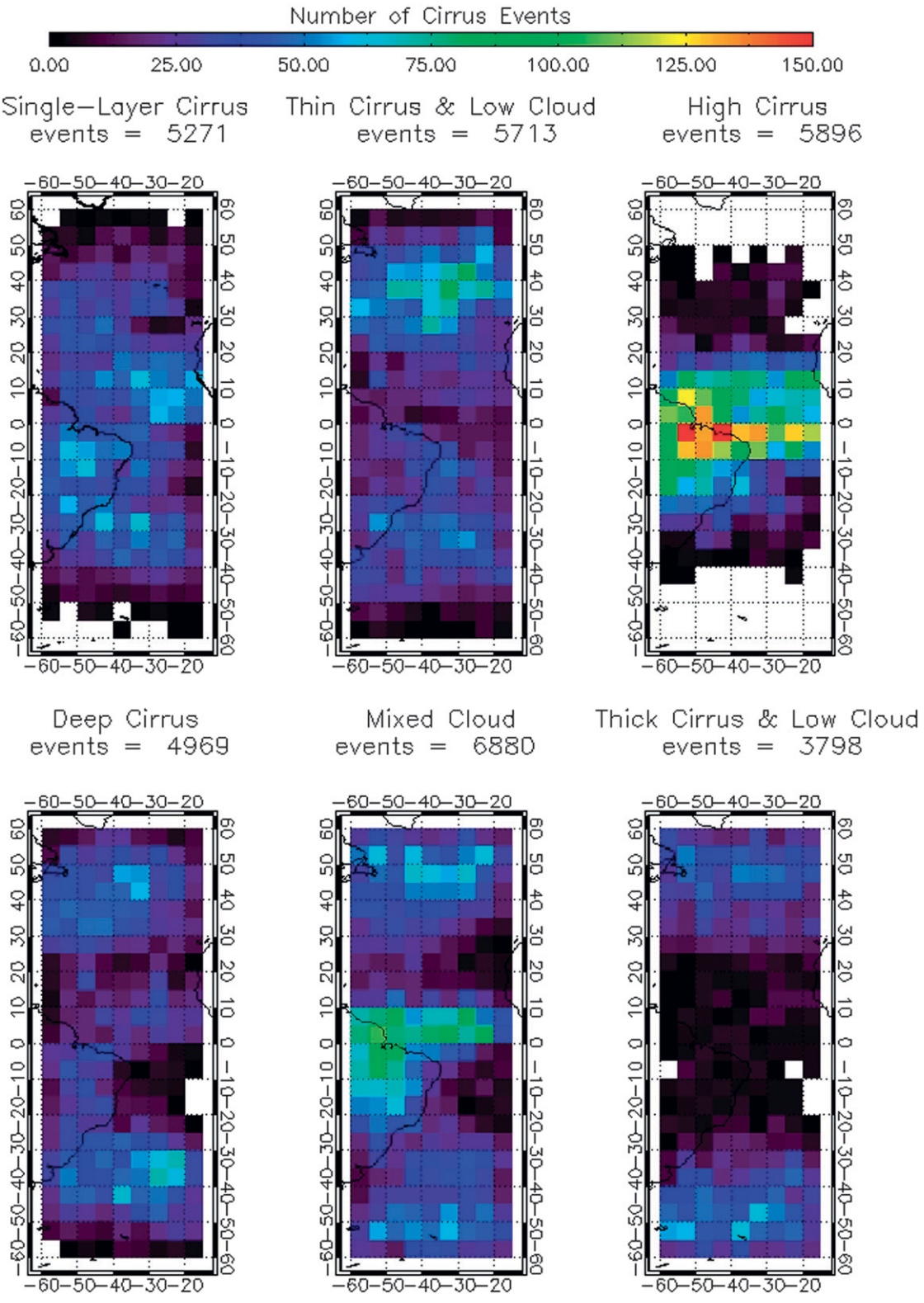

FIG. 5. The distributions of geographical locations of the cirrus events for each *P–Z* regime. The counts represent the number of cirrus events for each 5° × 5° region. Longitude is along the abscissa, and latitude is along the ordinate. Continental outlines are shown by black lines.

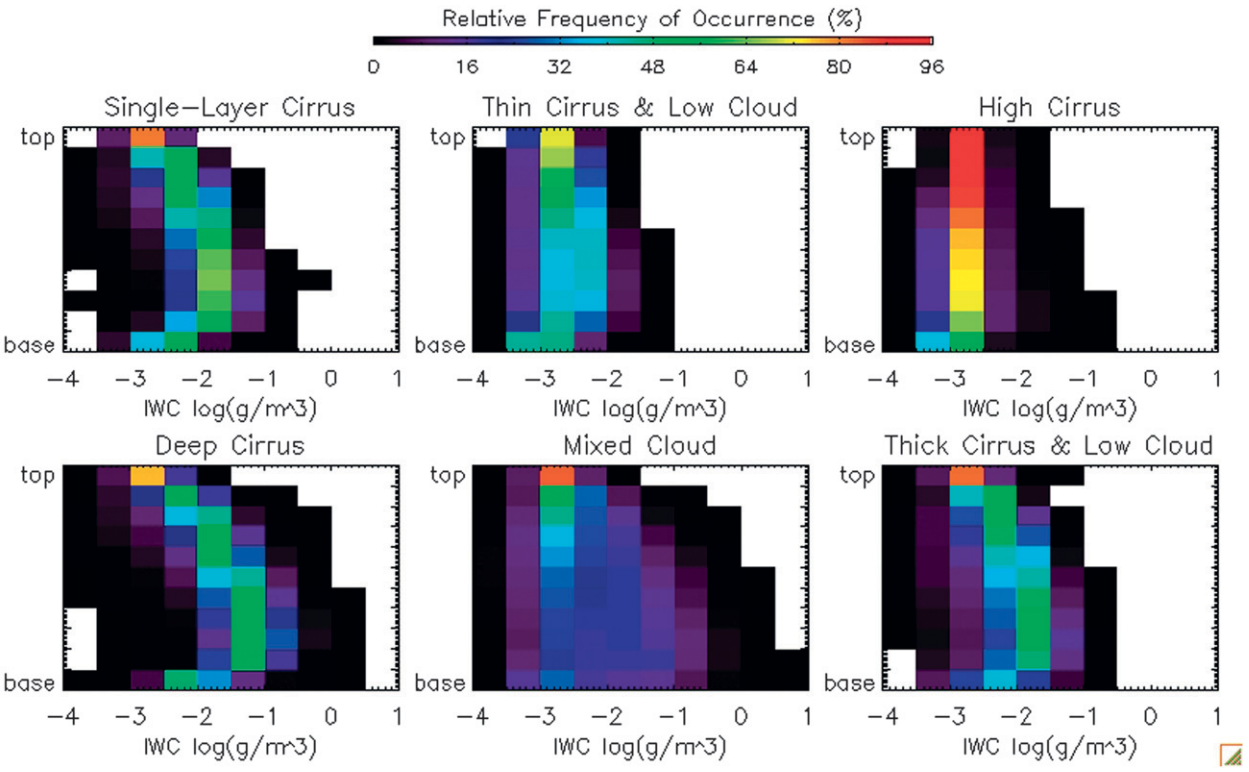

FIG. 6. Histograms of IWC, normalized by cloud depth, for the *P–Z* regimes.

occurs downstream of the regional maximum in ascent at 300 hPa, as shown in Fig. 7. Both deep cirrus and thick cirrus with low cloud exist in a southwesterly flow associated with a speed maximum at 300 hPa. The thick cirrus with low cloud is similar to the cirrostratus case documented by Sassen et al. (1989), which is found in strong southwesterly flow at upper levels (44 m s^{-1} at 9 km), has a low cloud base of 6 km, and has a deep cloud layer (6 km) with relatively small IWP (52 g m^{-2}). By comparison, thick cirrus with low cloud is also found in strong southwesterly flow at upper levels (30 m s^{-1} at 300 hPa), has a low cloud base (6.7 km), and is characterized by a thick cirrus layer (3.2 ± 1.8 km) with relatively small IWP (43 g m^{-2}).

The final two *P–Z* types are distinct from the others. They are composed of what appears to be primarily thin high cirrus that is restricted to the tropical tropopause layer and a regime that is characterized by clouds that are spread throughout the vertical column that we term mixed cloud (Fig. 4). The mixed cloud type appears not to be found in the subtropics (Fig. 5) and is likely a mixture of thick anvil cirrus and midlatitude frontal cirrus.

With the exception of the high cirrus type that is composed primarily of tropical tropopause-layer cirrus, all of the large-scale patterns are similar for the different *P–Z* types but with different degrees of intensity (Fig. 7; Table 3). One must keep in mind that the composite large-scale picture created here from the *P–Z* regimes is not necessarily the best rendering of the average dynamics because we are combining tropical cirrus with midlatitude cirrus to some degree in each composite. The cirrus that form the *P–Z* types exist, on average, in a southwesterly flow more or less ridgeward of the inflection point of a trough–ridge system. At 500 hPa, deep cirrus and mixed cloud coincide with a maximum in rising motion, whereas single-layer cirrus, thin cirrus with low cloud, and thick cirrus with low cloud are found downstream of the maximum rising motion (Fig. 7). A similar association with vertical motion was also found from analysis of data collected at the Atmospheric Radiation Measurement Program Southern Great Plains site (Mace et al. 2006a). It would appear that advection of condensate formed in ascending air upstream of the observation point plays an important role in the properties of the observed cirrus. Several of the *P–Z* types (thin cirrus with low cloud, thick cirrus with low cloud, and deep cirrus) are associated with the right exit quadrant of a jet streak where classical jet-stream dynamics would predict subsidence (Shapiro 1981) for a zonal jet but ascent for curved jet streaks (Shapiro and Kennedy 1981).

We find that the magnitude of the mean IWP of a *P–Z* type is strongly correlated with the vertical motion at the

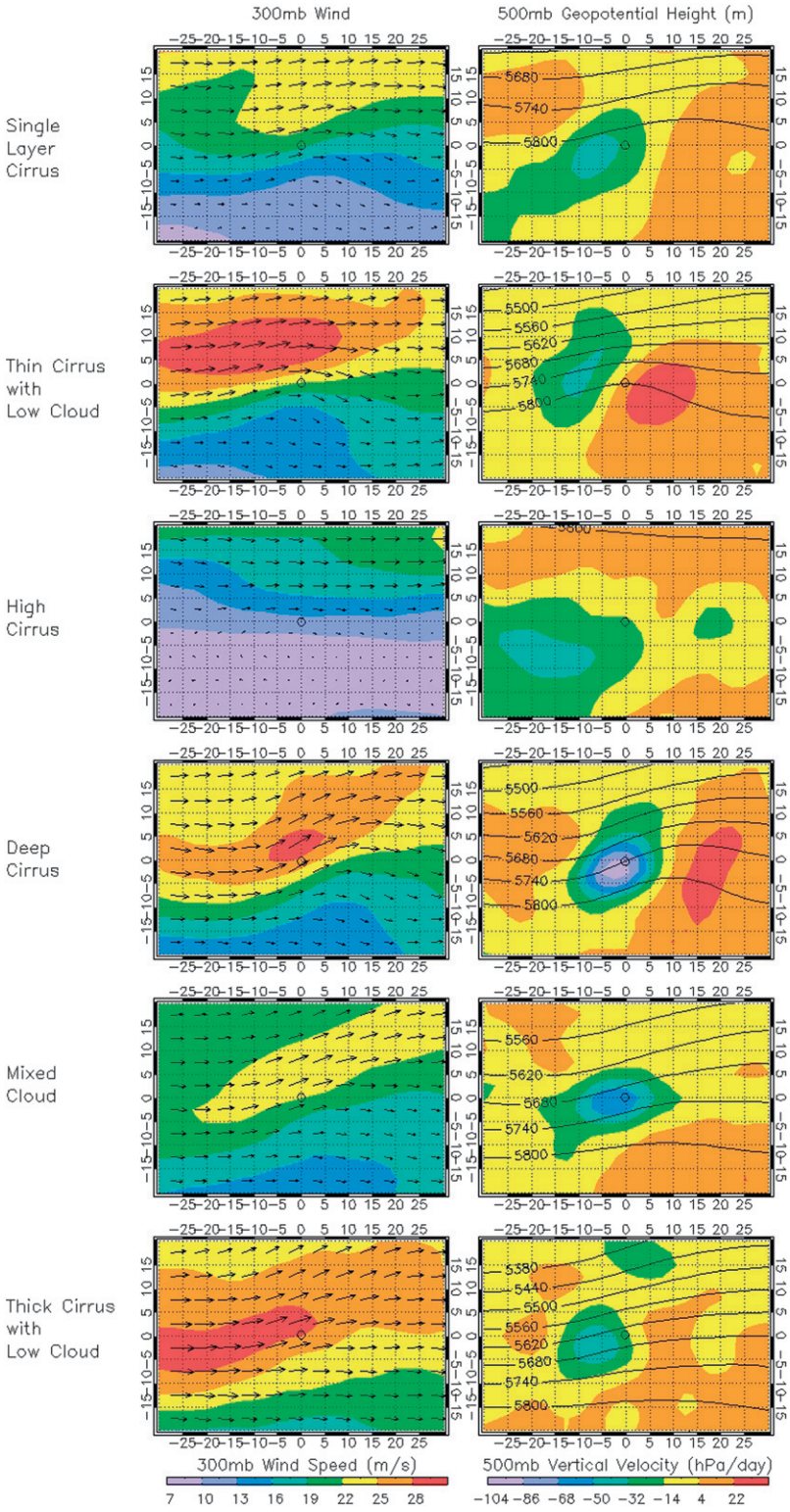

FIG. 7. Two-panel plots of the composite dynamics for each *P–Z* regime (Northern Hemisphere only) for (left) 300-hPa wind speed and direction and (right) 500-hPa geopotential heights and omega. The ordinate (latitude) and abscissa (longitude) are degrees relative to the cirrus event. The open circle at the origin of each panel denotes the location at which the cirrus was observed.

TABLE 3. Summary of the dynamic quantities for the *P–Z* regimes. Shown are the mean, the standard deviation, and the median (in parentheses) of the distribution of the quantity. Here, *w* is vertical wind speed.

	300-hPa *w* ($cm\ s^{-1}$)	300-hPa RH (%)	500-hPa *w* ($cm\ s^{-1}$)	500-hPa vorticity advection ($s^{-2} \times 10^{-10}$)	850-hPa temperature advection ($K\ s^{-1} \times 10^{-5}$)
Single-layer cirrus	+0.93 ± 2.36 (0.70)	43.9 ± 29.3 (41.0)	+0.58 ± 2.05 (0.35)	0.54 ± 6.34 (0.06)	0.16 ± 4.68 (−0.02)
Thin cirrus/low cloud	−0.02 ± 2.20 (−0.11)	49.0 ± 27.4 (50.0)	−0.08 ± 1.88 (−0.21)	0.47 ± 7.27 (0.20)	0.51 ± 5.41 (0.08)
High cirrus	+0.09 ± 2.22 (−0.11)	19.8 ± 18.5 (15.0)	+0.20 ± 2.02 (−0.07)	0.16 ± 3.61 (−0.006)	−0.14 ± 2.99 (−0.15)
Deep cirrus	+2.05 ± 2.57 (1.82)	64.4 ± 29.1 (72.0)	+1.61 ± 2.38 (1.38)	2.94 ± 10.18 (0.85)	0.62 ± 7.36 (0.29)
Mixed cloud	+1.12 ± 2.51 (0.79)	44.1 ± 31.6 (41.0)	+1.15 ± 2.40 (0.79)	1.56 ± 9.76 (0.32)	0.55 ± 7.01 (0.07)
Thick cirrus/low cloud	+0.58 ± 2.10 (0.38)	61.8 ± 27.6 (67.0)	+0.49 ± 2.04 (0.34)	1.46 ± 10.76 (0.90)	1.03 ± 7.21 (0.57)

point of measurement in the upper troposphere. If we simply correlate the mean IWP of the *P–Z* types (Table 2) with the corresponding mean vertical velocity (Table 3), we actually find that the IWP has a correlation coefficient of +0.95 with the vertical velocity. This association is interesting because these large-scale dynamical characteristics are entirely independent of the A-Train measurements used to create the composites and the dynamical values were not used in the creation of the composites. While the IWP itself is not independent of the *Z* values measured by *CloudSat* and used in the creation of the composites, this quantity is derived from an algorithm that includes other data sources in the A-Train (M10). Notable is that the relative humidity reported in the reanalysis product (Table 3) is much less strongly correlated (+0.54) with IWP (Table 2). This lack of correlation between water vapor and cloud properties is likely due to two reasons. First, the relative humidity is classified in the NCEP–NCAR reanalysis as a type-B variable, meaning that it is influenced by both observations and the model (including the model cloud parameterizations) and therefore is less reliable than variables that are strongly influenced by observations (type A). This fact points to a lack of model skill to predict water vapor since it is not strongly constrained by observations (especially in the upper troposphere). Second, the observed cirrus are advecting from upstream; therefore, the observed cirrus properties may be as related to the water vapor field in the region of formation as they are to the local conditions at the point of observation.

The results of the imagery pattern-tracking algorithm are listed in Table 4. On average about 2 times as many layers tend to be dissipating as there are layers that are becoming thicker with time. This statistic is intriguing because it suggests that cirrus, as we define them in this study, are tending to move away from dynamical support. Because we require these layers to be isolated from lower layers, it seems as though in many circumstances the cirrus are advecting downstream of the dynamics that created the deeper cloud layers from which these layers are derived. This possibility seems especially true in the thin cirrus with low cloud, for which the growing-to-dissipating ratio is only 0.38. The exception to this finding is the mixed cloud regime for which the growing-to-dissipating ratio is 0.71, suggesting that a greater fraction of these apparently dynamically active layers are developing. It is unknown at this point whether this phenomenon is due to there being a greater fraction of tropical anvil cirrus in this composite.

b. Cirrus regimes defined by large-scale dynamics

Six regimes appear to be sufficient to describe the different types of dynamical conditions that tend to produce cirrus clouds in the A-Train data in the Atlantic basin region. Tables 5 and 6 summarize the bulk properties and mean dynamics for the dynamical regimes and Fig. 8 shows the large-scale meteorological environment for the dynamics regimes. Figure 9 shows the geographic distributions of the regimes, and Figs. 10 and 11 show, respectively, the *P–Z* patterns of the regimes and the

TABLE 4. Tracking statistics for *P–Z* regimes. Each column denotes the number of events for the *P–Z* type that had a water vapor channel Tb that was getting steadily colder (growing), had a Tb that was getting steadily warmer (dissipating), or whose Tb was either fluctuating or unchanging during the time of tracking. See text for further details.

	Growing	Dissipating	Steady	Growing/dissipating ratio
Single-layer cirrus	608	1488	419	0.41
Thin cirrus with low cloud	575	1524	585	0.38
High cirrus	622	1149	836	0.54
Deep cirrus	574	1204	462	0.48
Mixed cloud	999	1406	692	0.71
Thick cirrus with low cloud	460	847	371	0.54

normalized vertical distributions of IWC. Of these regimes, we find that two of the regimes are principally found in the tropics, two of the regimes are associated with events in the subtropics, and two regimes correspond to midlatitude situations. From Fig. 9 it is apparent that ridge-crest cirrus is the dominant type in both the subtropics and the midlatitudes. Because more ridge-crest cirrus events occur between ±25° and 40° latitude than between ±40° and 60° latitude, however, we consider the ridge-crest regime to be a subtropical regime. The frequencies of occurrence of these regimes are a strong function of latitude, with the tropical regimes dominating the total number of cases. The primary differences between the pairs in each latitude band seem to be associated with the intensity of the dynamics as quantified in Table 6. From the broad characteristics of these regimes and the character of the cirrus found within them, we assign descriptive names, as illustrated in the tables and figures just referenced. For each dynamics regime we show the distribution of the *P–Z* morphological types in Fig. 12. Since the cloud macrophysical and microphysical properties are largely determined by the *P–Z* type, examining how the types are distributed among the dynamics regimes is instructive for understanding the coupling between the large-scale meteorological environment and the life cycle and properties of cirrus cloud systems that develop within the dynamics regimes. The case study shown in Figs. 1–3, for instance, is a member of the ridge-crest dynamics regime, and, at 164 g m^{-2}, the IWP of this case is within 1 standard deviation of the mean IWP of the ridge-crest type.

Although it is difficult to identify a predominant pattern from Fig. 12, we can take away several lessons from it. Within each dynamics regime we find some occurrence of most morphological types; within each dynamics regime, however, certain combinations of morphological types are predominant. This result suggests that the properties of cirrus cloud systems are not necessarily static within large-scale regimes but that the cirrus cloud systems evolve through life cycles that describe some combination of our morphological types depending on the dynamics regime. This situation implies that simple parameterizations of cirrus properties from the resolved-scale dynamics alone will not be able to capture the details of cirrus cloud microphysics and radiative forcing. It is evident from Fig. 12, however, that certain combinations of morphological types are more strongly associated with certain dynamics regimes, suggesting that the large-scale dynamics drives variability in the meso- and smaller-scale motions that govern the life cycles of cirrus systems (e.g., Sassen et al. 1989).

The tropical regimes demonstrate weak large-scale dynamics overall as expected. There is a clear difference

TABLE 5. Bulk properties of the cirrus events in the dynamics regimes. Cell contents are as in Table 1.

	Deep wave	Developing tropical	Subtropical jet	Jet stream/prefrontal	Dissipating tropical	Ridge crest
Top (km)	10.5 ± 1.6 (10.6)	13.7 ± 2.5 (14.1)	12.2 ± 2.0 (12.1)	10.8 ± 1.6 (11)	13.2 ± 2.5 (13.5)	11.6 ± 1.7 (11.6)
Base (km)	6.3 ± 2.6 (6.3)	10.4 ± 3.1 (10.7)	8.1 ± 2.7 (7.8)	6.8 ± 2.7 (7)	10.6 ± 3.0 (10.8)	8.2 ± 2.4 (8.3)
Thickness (km)	4.2 ± 2.2 (3.9)	3.3 ± 2.3 (2.7)	4.2 ± 2.3 (3.9)	4.0 ± 2.4 (3.6)	2.7 ± 1.9 (2.1)	3.3 ± 2.0 (2.9)
Top temperature (°C)	−56.0 ± 7.9 (−56.7)	−67.1 ± 11.8 (−69.2)	−59.6 ± 10.5 (−59.5)	−57.1 ± 7.8 (−58.1)	−65.2 ± 11.9 (−66.1)	−57.9 ± 9.0 (−58.3)
Base temperature (°C)	−26.5 ± 14.8 (−25.0)	−42.9 ± 19.3 (−43.7)	−29.3 ± 16.7 (−27.3)	−29.0 ± 15.9 (−29.4)	−46.1 ± 17.9 (−46.8)	−33.5 ± 15.2 (−33.4)
Max (dBZ) temperature (°C)	−34.6 ± 13.5 (−33.7)	−51.1 ± 17.6 (−51.9)	−38.0 ± 15.4 (−36.0)	−36.7 ± 14.9 (−37.4)	−53.4 ± 16.2 (−54.4)	−41.3 ± 13.9 (−41.4)
Ice water path (g m^{-2})	165.7 ± 259 (70.5)	90.4 ± 212 (14.0)	155.9 ± 243 (63.9)	122.1 ± 217 (36.6)	47.8 ± 142 (7.4)	74.6 ± 147 (25.5)

TABLE 6. Summary of the large-scale dynamics associated with the six dynamics regimes. Shown are the mean, the standard deviation, and the median (in parentheses) of the distribution of the quantity. Positive values of temperature advection represent warm-air advection.

	300-hPa w (cm s^{-1})	300-hPa RH (%)	500-hPa w (cm s^{-1})	500-hPa vorticity advection ($s^{-2} \times 10^{-10}$)	850-hPa temperature advection (K $s^{-1} \times 10^{-5}$)
Dissipating tropical	−1.25 ± 1.39 (−1.08)	26.3 ± 19.3 (23.0)	−1.05 ± 1.23 (−0.92)	−1.07 ± 6.16 (−0.22)	−0.74 ± 4.04 (−0.26)
Deep wave	2.49 ± 2.32 (2.16)	76.4 ± 20.9 (82.0)	2.93 ± 2.35 (2.61)	20.96 ± 10.04 (18.25)	−1.69 ± 9.99 (−0.50)
Developing tropical	2.00 ± 1.73 (1.68)	19.6 ± 15.5 (18.0)	1.48 ± 1.46 (1.23)	0.33 ± 3.96 (0.11)	−0.40 ± 3.13 (−0.11)
Subtropical jet	3.84 ± 2.40 (3.50)	73.4 ± 22.0 (79.0)	3.43 ± 2.54 (3.05)	0.80 ± 6.66 (0.66)	−0.08 ± 6.06 (0.37)
Jet stream/prefrontal	0.75 ± 2.02 (0.61)	74.8 ± 19.8 (79.0)	1.07 ± 2.00 (0.86)	1.31 ± 10.48 (1.68)	12.98 ± 5.97 (11.39)
Ridge crest	0.49 ± 1.31 (0.49)	75.1 ± 14.8 (76.0)	0.25 ± 1.23 (0.25)	−0.25 ± 6.48 (0.05)	−0.19 ± 4.14 (0.18)

in the large-scale vertical motion that emerges from the cluster analysis, however. Table 6 shows that the regime that is labeled as dissipating tropical cirrus has strong descent at 300 hPa whereas the regime that is called developing tropical cirrus demonstrates upward vertical motion. Because only the occurrence of cirrus and not its microphysical or macrophysical properties were used in developing these composites, it is interesting to examine whether the bulk properties correspond to the overall character of the dynamics regimes. Overall, we do find this correspondence. While the tropical cirrus in both regimes are clearly higher and colder and contain much less condensate when compared with all of the other regimes, the information from Table 5 reveals that the dissipating regime is found to have less IWP by about a factor of 2 (average of 48 g m^{-2}) in layers that are slightly lower and thinner relative to the developing regime where the IWP average is 90 g m^{-2}. Note that the IWP distributions are noticeably skewed to small values in both tropical regimes although the distributions are broad. From Fig. 11, we find that the vertical distribution of IWC is more weighted to the top half of the layer in the developing regime as would be expected from younger, more dynamically active clouds. Of the layers tracked with the water-imagery-pattern-matching algorithm, there tend to be more layers that are thinning with time in the dissipating regime by about a factor of 3, whereas the ratio is somewhat smaller (a factor of 2) in the developing regime (Table 7).

Given these characteristics, it is likely that these tropical regimes include everything from relatively fresh anvils to very thin cirrus in the tropical tropopause layer (TTL). This contention is borne out by examining the anomalies of *P–Z* types that are found in the tropical regimes, as shown in Fig. 12. Both regimes demonstrate a positive anomaly of high cirrus relative to the background state, with high cirrus being only slightly more common in the dissipating regime. High cirrus is found primarily in the TTL, between 13.5 and 15.5 km (Table 2). These thin TTL cirrus are typically disconnected dynamically from tropospheric cirrus that is more directly associated with the convection (Comstock et al. 2002; Schwartz and Mace 2010). The developing regime, on the other hand, is more likely to contain *P–Z* types with larger IWP and *P–Z* types that often exist with lower-level clouds such as mixed, single-layer, and thick cirrus with low cloud. The larger RFO of the thicker cirrus types for developing tropical cirrus comes at the expense of thin cirrus with low cloud, which is significantly more common in the dissipating regime. The differences in morphological types within these two dynamics regimes suggest that cirrus make a transition from anvils and dynamically forced cirrus in the developing regime to cirrus that have moved beyond their dynamical support in the dissipating regime.

The subtropical-jet regime is characterized by very strong dynamical forcing relative to the more quiescent ridge-crest regime. In the ridge-crest regime we find very weak ascent in the mid- and upper troposphere (Table 6). The subtropical-jet regime dynamical state is characterized by strong ascent (+4 cm s^{-1}) at 300 hPa. Also, we find that subtropical-jet cirrus events are slightly more likely to be thickening with time than are ridge-crest cirrus during the period of tracking (Table 7). With the subtropical-jet cirrus located in a stronger southwesterly flow (Fig. 8), the mean 500-hPa vorticity advection is slightly positive as compared with the weak negative vorticity advection in the ridge-crest regime (Table 6). Figure 10 shows that the cirrus systems that occur in the subtropical-jet regime tend to occur often with lower cloud layers that can have large radar reflectivity, unlike the ridge-crest cases that are predominantly single layer with infrequent boundary layer clouds. It is not surprising, given these characteristics, that the types labeled as mixed cloud and thick cirrus with low cloud are much more frequent in the subtropical-jet regime relative to the ridge-crest regime, in which single-layer cirrus is more common, as shown in Fig. 12. We do find that deep cirrus is actually more common in the ridge-crest regime than in the subtropical-jet regime.

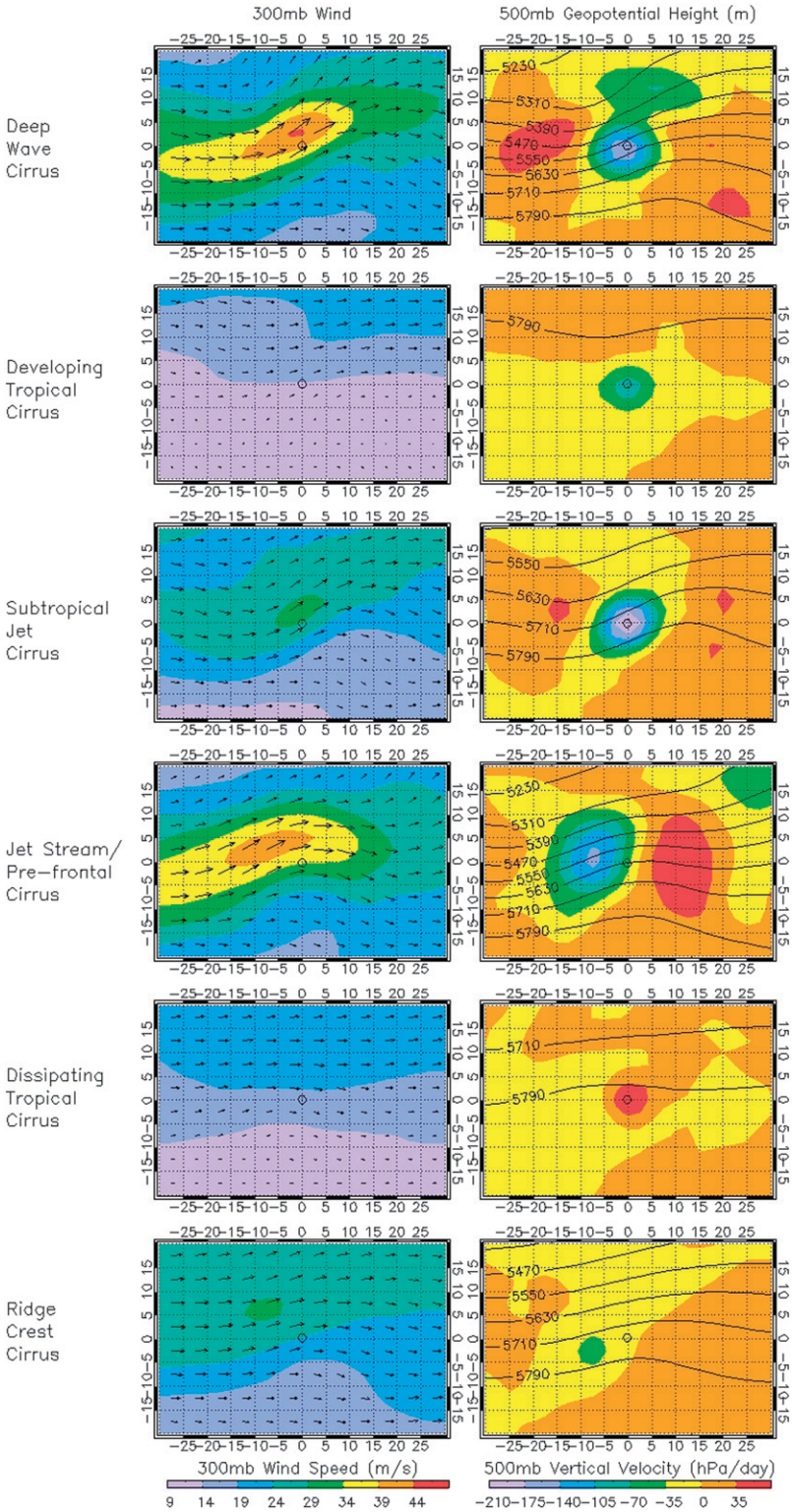

FIG. 8. As in Fig. 7, but for each dynamics regime.

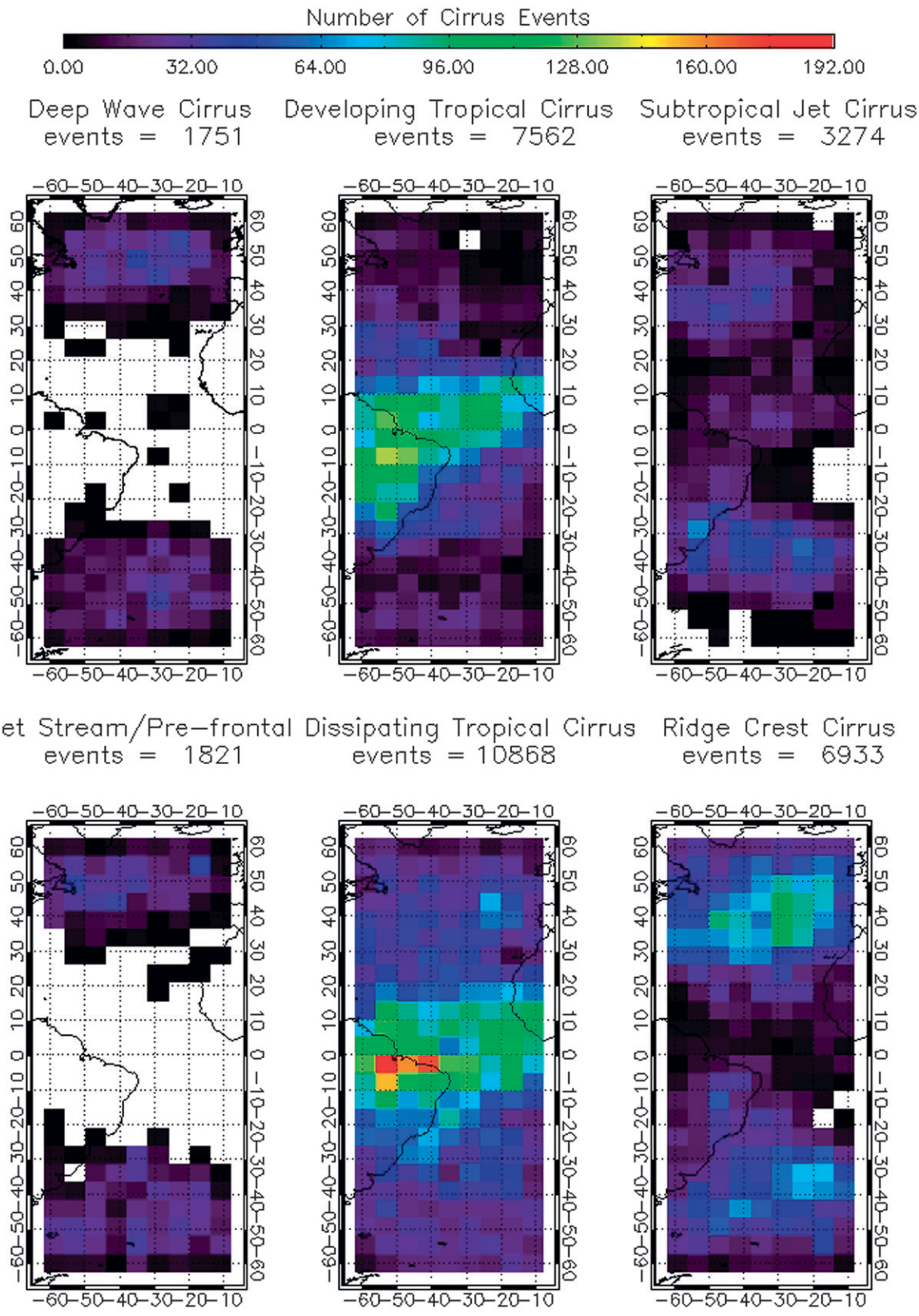

FIG. 9. As in Fig. 5, but for each dynamics regime.

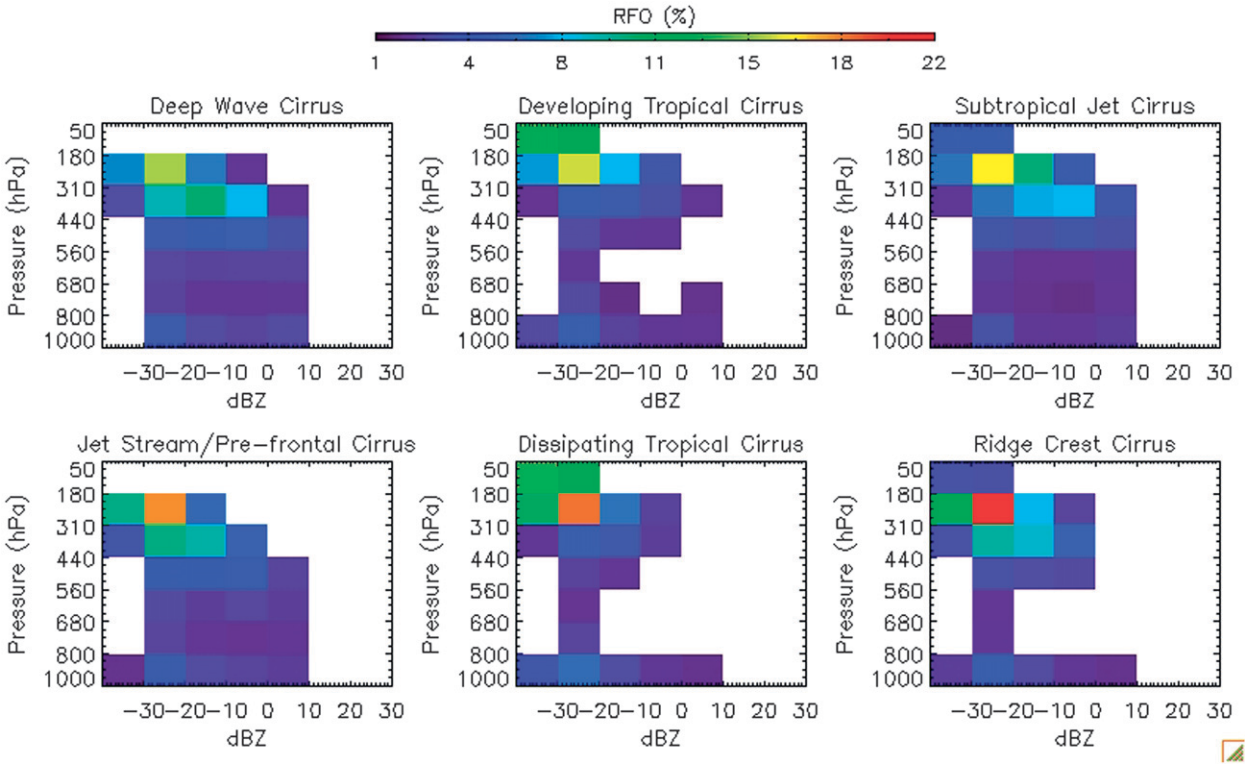

FIG. 10. As in Fig. 4, but for the six dynamics regimes.

Deep cirrus is characterized by large IWP (Table 2) but few low-level clouds (Fig. 10). It seems likely that these heavy isolated cirrus layers are associated with strong warm fronts that have penetrated into the subtropics and have tapped humid upper-tropospheric air from lower latitudes. The bulk properties of the cirrus are commensurate with the dynamics. The geometrical locations of the layers in the two regimes are similar, but the subtropical-jet cirrus layers are about 1 km thicker, with IWP that is larger by about a factor of 2 than that of the ridge-crest cirrus (Table 5). The variability of the IWP in the ridge-crest regime is about one-third larger than is found in the subtropical-jet regime, however.

At high latitudes, well-defined jet streams characterize both regimes, although the regime labeled deep-wave cirrus has much more intense dynamics overall. The deep-wave regime is primarily indicated by very strong positive vorticity advection, which is associated with 300- and 500-hPa ascent (Table 6). Interesting is that we find cold-air advection and northwesterly flow in the lower troposphere of this regime, suggesting that at times this regime is found behind a cold front in the lower troposphere. The dynamics of what we term jet-stream/prefrontal cirrus tends to be weaker overall, although strong warm-air advection is noted in the lower troposphere, suggesting that this regime may be found predominantly in the warm sector of midlatitude cyclones. The pattern of vertical motion differs between these regimes also. The jet-stream/prefrontal cirrus tends to be observed downstream of the maximum in upper-tropospheric ascent very near the right front exit region of the jet streak, whereas the cirrus associated with the deep-wave regime tends to be observed very near the center of ascent and closer to the right entrance region of the jet streak (Fig. 8). Deep-wave cirrus has the highest percentage of thickening cirrus events, as determined by the water vapor–tracking algorithm, with nearly an equal frequency of thinning and thickening events, whereas thinning events are 2 times as likely as thickening events for jet-stream/prefrontal cirrus (Table 7). The bulk properties of the cirrus correspond to the dynamical differences, although these differences are not quite as dramatic as are found in the lower-latitude regimes. The cirrus in both regimes tends to have similar geometrical boundaries and temperature occurrences, and the deep-wave cirrus has slightly greater mean IWP with a much greater median value of IWP (Table 5). This larger IWP corresponds to a vertical distribution of IWC in the deep-wave regime that is notably broader in the lower third of the layer when compared with that of the jet-stream/prefrontal regime (Fig. 11). Lower-level mid- and lower-tropospheric layers are common in both regimes, although

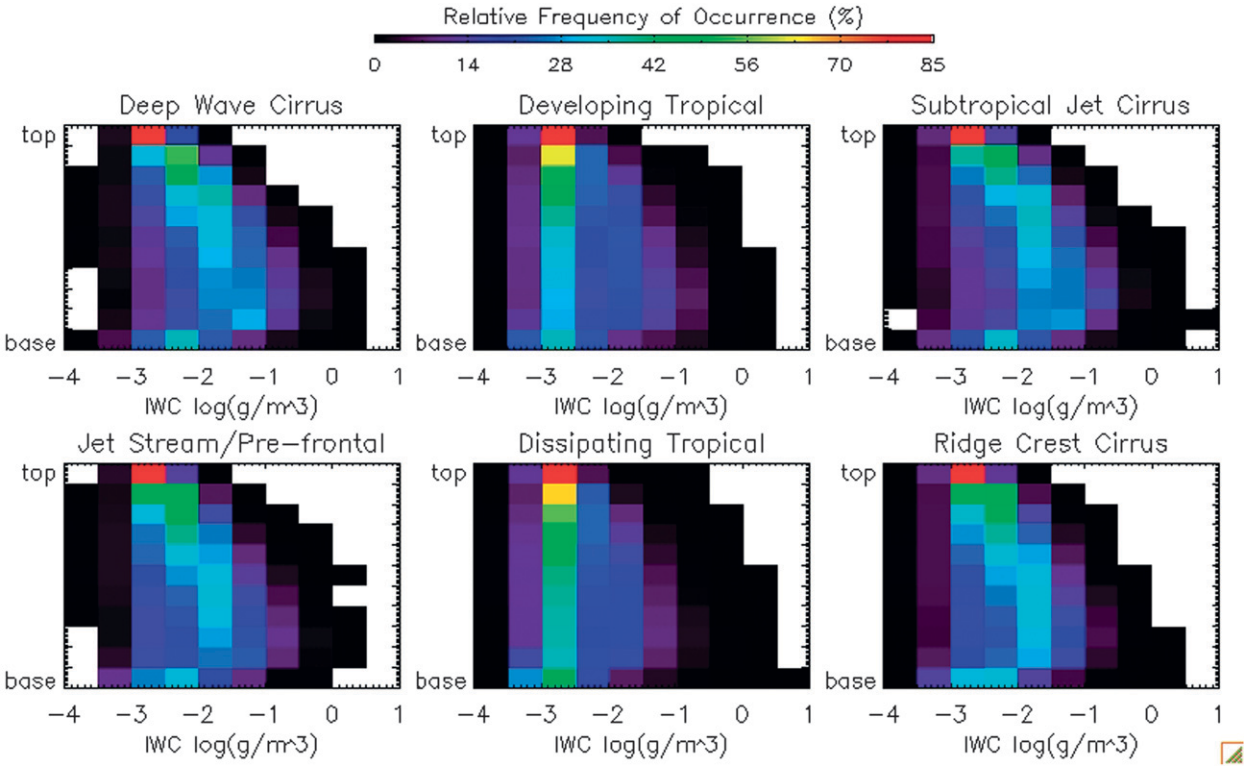

FIG. 11. As in Fig. 6, but for the dynamics regimes.

they are more common in the deep-wave regime (Fig. 10).

The morphological types that occupy these midlatitude regimes are similar in many respects, as shown in Fig. 12. Both regimes have similar relative frequencies of mixed cloud, deep cirrus, and single-layer cirrus. There is relatively more thick cirrus with low cloud found in the deep-wave dynamical regime than is found in the jet-stream/prefrontal regime, for which more thin cirrus with low cloud type occurs. We interpret these results as suggesting that cirrus layers that are moving through the dynamical pattern evolve from more dynamically active situations in the vicinity of the frontal boundaries in midlatitude waves where IWP is larger in geometrically thicker layers to situations in which the dynamics is less strong and the cirrus is less thick downstream of the inflection point in the flow pattern.

4. Summary

By exploiting the synergy of the active instruments on the A-Train satellites and by combining the A-Train data with time sequences of geostationary satellite data and meteorological reanalysis data, we are able to examine the relationships among the dynamical and morphological characteristics of cirrus over a broad region. Cirrus events are identified using a merged *CloudSat–CALIPSO* hydrometeor occurrence product known as radar–lidar (RL)-GEOPROF (Mace et al. 2009). The synergy between the cloud radar on *CloudSat* and the optical lidar on *CALIPSO* allows us to identify thick cirrus that would attenuate the lidar and tenuous cirrus that has a radar reflectivity below the detection threshold of the *CloudSat* CPR. In this study, over 30 000 cirrus events (defined to be 250-km segments with more than 75% cirrus) are extracted from data collected over the Atlantic basin in 2007 in a domain that extends from the Southern Hemisphere midlatitudes to the Northern Hemisphere midlatitudes. This dataset includes a broad continuum of upper-tropospheric clouds in a similarly broad range of large-scale meteorological situations (Table 1). To make sense of this dataset, we attempt to identify characteristic patterns in the cloud morphology and large-scale meteorological environment by applying a cluster-analysis algorithm to P–Z histograms and to the large-scale dynamics in which the cirrus events are observed.

We identify six regimes using the P–Z histograms that appear to separate the macrophysical and bulk microphysical properties of the cloud systems into distinct populations (Figs. 4–7 and Tables 2–4). In decreasing order of their mean ice water path, these morphological types are identified as follows:

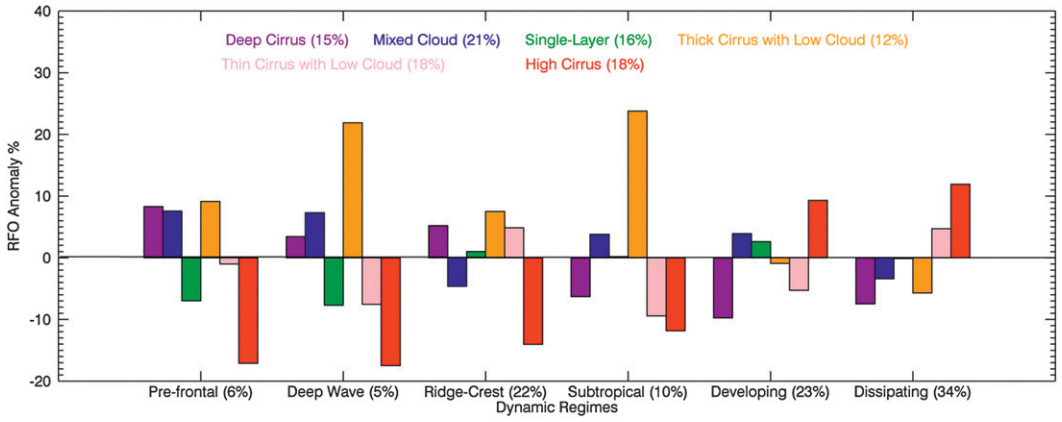

FIG. 12. The anomaly of *P–Z* regime membership for each dynamics regime in comparison with the background state (all cirrus events) of *P–Z* regimes, which is shown across the top of the plot. A negative (positive) RFO anomaly means that the given *P–Z* regime is less (more) likely to occur in that dynamic state than in the background state. The RFO for each dynamics regime is shown on the *x* axis. The order from left to right of *P–Z* regimes goes from highest to lowest IWP. The *P–Z* regime membership for each dynamics regime can be determined by adding the RFO anomaly to the background state. Within each dynamics regime, the RFO anomaly sums to zero. The RFO of the dynamics regime multiplied by the RFO anomaly for a given *P–Z* regime sums to zero across the dynamics regimes.

1) Deep cirrus (RFO = 15%; IWP = 263 ± 255 g m^{-2}) tends to occur in regions of strongest ascent (+2.05 cm s^{-1}) throughout the analysis domain and is typically found in isolated layers with few other lower-level clouds.
2) Mixed cloud (RFO = 21%; IWP = 141 ± 283 g m^{-2}) is found in regions of ascent (+1.12 cm s^{-1}) and appears not to be frequent in the subtropics but is widespread in the midlatitudes and the equatorial zone. This type includes cirrus layers that coexist with mid- and lower-level cloud layers.
3) Single-layer (RFO = 16%; IWP = 48 ± 53 g m^{-2}) regime is found throughout the analysis domain and in regions of weak ascent (+0.93 cm s^{-1}); these clouds occur primarily in isolated layers with only sparse lower-level clouds.
4) Thick cirrus with low cloud (RFO = 12%; IWP = 43 ± 45 g m^{-2}) is found primarily in the midlatitudes of both hemispheres in areas of weak ascent (+0.58 cm s^{-1}); these layers are found through a deep upper-tropospheric layer and often occur with mid- and low-level clouds.
5) Thin cirrus with low cloud (RFO = 18%; IWP = 8 ± 8 g m^{-2}) is found primarily in the subtropics of both hemispheres in regions of near neutral ascent; these optically and geometrically thin layers often occur above boundary layer clouds.
6) High cirrus (RFO = 18%; IWP = 5 ± 15 g m^{-2}) is found exclusively in the tropics and as thin layers that are based above 13 km. These clouds are principally TTL cirrus.

To characterize the meteorological conditions in which cirrus clouds are observed, we apply the *K*-means algorithm to the large-scale dynamical variables associated with the cirrus events. In this analysis, the cloud properties were not used in the cluster analysis so that the properties would be independent of the cluster-analysis results. We again identify six regimes that appear to reasonably capture much of the variability in the large-scale states that give rise to cirrus layers (Figs. 8–11 and Tables 5 and 6). Two of these regimes are principally in the tropics, two are in the subtropics, and two are in the midlatitudes. Although ridge-crest cirrus has a prominence in both the subtropics and midlatitudes, we consider it to be a subtropics regime here. In each of these pairs one regime tends to be more strongly forced than the other, and in each pair the more strongly forced regime has much greater IWP and tends to have a larger fraction of events that are becoming deeper during the 6 h centered on the A-Train overpass, as determined by

TABLE 7. As in Table 4, but for the dynamics regimes.

	Growing	Dissipating	Steady	Growing/ dissipating ratio
Deep wave	287	323	189	0.89
Developing tropical	927	1800	731	0.52
Subtropical jet	482	737	302	0.65
Prefrontal	210	374	180	0.56
Dissipating tropical	987	2727	1225	0.36
Ridge crest	905	1587	709	0.57

tracking the cirrus regime using geostationary satellite sequences. By examining the *P–Z* morophological regimes that populate these dynamics regimes, we find the following:

1) In the tropical regimes, a background state of high cirrus exists in equal proportions within the dissipating and developing tropical dynamics regimes. The differences between the more strongly forced developing tropical regime and the dissipating regime were found among the tropospheric cirrus. Additional research will be required to determine whether the developing tropical cirrus regime is associated more directly with active convection and anvil outflows. Morphological types that tended to have higher IWP such as mixed cloud and thick cirrus with low cloud were found more frequently in the developing regime where large-scale vertical motion was positive.
2) In the subtropics of both hemispheres, the more strongly forced subtropical-jet regime had an overall higher frequency of occurrence of mixed cloud and thick cirrus with low cloud whereas the ridge-crest regime tended to have weaker large-scale ascent and cirrus types with less IWP, such as single-layer cirrus.
3) In the midlatitudes we identify dynamics regimes that we term deep-wave and jet-stream/prefrontal cirrus. The deep-wave regime seems to exist in the vicinity of the cold front of midlatitude baroclinic waves and the jet-stream/prefrontal cirrus seems to exist upstream in the warm sector of these systems. The differences in the cirrus found in these regimes are subtle, with both regimes having about the same relative frequencies of mixed cloud, deep cirrus, and single-layer cirrus. The deep-wave regime tends to have more thick cirrus with low cloud, and the jet-stream/prefrontal regime tends to have more thin cirrus with low cloud.

Overall, these results are consistent with the assumption that the properties of cirrus cloud systems in a gross sense are correlated with the large-scale environments in which they exist. The morphological types show a consistent relationship between IWP and large-scale ascent. When viewed in terms of dynamics regimes, a coherent relationship is found between the large-scale forcing and the cirrus types that populate them. The degree to which the large-scale meteorological environment and gross cirrus properties are correlated appears to be due to the fact that the large scale governs the meso- and smaller-scale dynamics that ultimately drive the formation and dissipation of cloud elements (Sassen et al. 1989). The results suggest that, as condensate responds to and passes through the dynamics regimes, the identifiable cirrus cloud systems evolve through various states that can be linked to the large-scale meteorological environment. We speculate from the variability of cloud properties within the dynamics regimes (Fig. 12) that the details of cirrus evolution within the regimes are a function of the local meso- and smaller-scale meteorological conditions (i.e., Comstock et al. 2008). Consistent with this assertion, efforts to develop cirrus parameterizations for large-scale models are focusing on the subgrid variability of supersaturation driven by unresolved turbulent motions (e.g., Kärcher and Burkhardt 2008; Kärcher 2012; Morrison and Gettelman 2008). Our findings in this paper support this approach to parameterization development.

Acknowledgments. This research has been supported primarily by National Aeronautics and Space Administration (NASA) Grants NNX10AM42G and NNX07AT45G and by a grant from the Jet Propulsion Laboratory, California Institute of Technology, under contract with NASA. We acknowledge the efforts of the engineers and scientists at the Jet Propulsion Laboratory, NASA Langley Research Center, Centre National d'Etudes Spatiales, Ball Aerospace, and the Cooperative Institute for Research in the Atmosphere, without whom the *CloudSat* and *CALIPSO* projects would not have been successful. In particular we acknowledge the efforts of Drs. Pat Minnis and Rabindra Palikonda at the NASA Langley Research Center who graciously provided the geostationary satellite data used in this study. An allocation of computer time from the Center for High Performance Computing at the University of Utah is gratefully acknowledged. Sally Benson at the University of Utah assisted in preparation of data and creation of figures.

REFERENCES

Anderberg, M. R., 1973: *Cluster Analysis for Applications.* Academic Press, 399 pp.

Bony, S., and J.-L. Dufresne, 2005: Marine boundary layer clouds at the heart of tropical cloud feedback uncertainties in climate models. *Geophys. Res. Lett.,* **32,** L20806, doi:10.1029/2005GL023851.

Comstock, J. M., T. P. Ackerman, and G. G. Mace, 2002: Ground-based lidar and radar remote sensing of tropical cirrus clouds at Nauru Island: Cloud statistics and radiative impacts. *J. Geophys. Res.,* **107,** 4714, doi:10.1029/2002JD002203.

——, R-F. Lin, D. O'C. Starr, and P. Yang, 2008: Understanding ice supersaturation, particle growth, and number concentration in cirrus clouds. *J. Geophys. Res.,* **113,** D23211, doi:10.1029/2008JD010332.

Dufresne, J.-L., and S. Bony, 2008: An assessment of the primary sources of spread of global warming estimates from coupled atmosphere–ocean models. *J. Climate,* **21,** 5135–5144.

Gordon, N. D., and J. R. Norris, 2010: Cluster analysis of midlatitude oceanic cloud regimes—Part 1: Mean cloud and

meteorological properties. *Atmos. Chem. Phys. Discuss.,* **10,** 1559–1593.

——, ——, C. P. Weaver, and S. A. Klein, 2005: Cluster analysis of cloud regimes and characteristic dynamics of midlatitude synoptic systems in observations and a model. *J. Geophys. Res.,* **110,** D15S17, doi:10.1029/2004JD005027.

Heymsfield, A. J., 1977: Precipitation development in stratiform ice clouds. *J. Atmos. Sci.,* **34,** 367–381.

Im, E., S. L. Durden, and C. Wu, 2006: Cloud profiling radar for the *CloudSat* mission. *IEEE Aerosp. Electron. Syst. Mag.,* **20,** 15–18.

Jakob, C., 2003: Objective identification of cloud regimes in the tropical western Pacific. *Geophys. Res. Lett.,* **30,** 2082, doi:10.1029/2003GL018367.

——, G. Tselioudis, and T. Hume, 2005: The radiative, cloud, and thermodynamic properties of the major tropical western pacific cloud regimes. *J. Climate,* **18,** 1203–1214.

Kalnay, E., and Coauthors, 1996: The NCEP/NCAR 40-Year Reanalysis Project. *Bull. Amer. Meteor. Soc.,* **77,** 437–471.

Kärcher, B., 2012: Supersaturation fluctuations in cirrus clouds driven by colored noise. *J. Atmos. Sci.,* **69,** 435–444.

——, and U. Burkhardt, 2008: A cirrus cloud scheme for general circulation models. *Quart. J. Roy. Meteor. Soc.,* **134,** 1439–1461.

Kistler, R., and Coauthors, 2001: The NCEP-NCAR 50-Year Reanalysis: Monthly means CD-ROM and documentation. *Bull. Amer. Meteor. Soc.,* **82,** 247–267.

Mace, G. G., 2010: Cloud properties and radiative forcing over the maritime storm tracks of the Southern Ocean and North Atlantic as derived from A-Train. *J. Geophys. Res.,* **115,** D10201, doi:10.1029/2009JD012517.

——, and S. Benson, 2008: The vertical structure of cloud occurrence and radiative forcing at the SGP ARM site as revealed by 8 years of continuous data. *J. Climate,* **21,** 2591–2610.

——, D. O'C. Starr, T. P. Ackerman, and P. Minnis, 1995: Examination of coupling between an upper tropospheric cloud system and synoptic scale dynamics diagnosed from wind profiler and radiosonde data. *J. Atmos. Sci.,* **52,** 4094–4127.

——, S. Benson, and E. Vernon, 2006a: On the relationship between cirrus cloud occurrence and microphysical properties with the large-scale atmospheric state revealed by six years of continuous ground-based cloud radar data. *J. Climate,* **19,** 3257–3278.

——, and Coauthors, 2006b: Cloud radiative forcing at the ARM Climate Research Facility: Part 1. Technique, validation, and comparison to satellite-derived diagnostic quantities. *J. Geophys. Res.,* **111,** D11S90, doi:10.1029/2005JD005921.

——, M. Deng, B. J. Soden, and E. Zipser, 2006c: Association of tropical cirrus in the 10–15-km layer with deep convective sources: An observational study combining millimeter radar data and satellite-derived trajectories. *J. Atmos. Sci.,* **63,** 480–503.

——, Q. Zhang, M. Vaughn, R. Marchand, G. Stephens, C. Trepte, and D. Winker, 2009: A description of hydrometeor layer occurrence statistics derived from the first year of merged *CloudSat* and *CALIPSO* data. *J. Geophys. Res.,* **114,** D00A26, doi:10.1029/2007JD009755.

Morrison, H., and A. Gettelman, 2008: A new two-moment bulk stratiform cloud microphysics scheme in the Community Atmosphere Model, version 3 (CAM3). Part 1: Description and numerical tests. *J. Climate,* **21,** 3642–3660.

Parkinson, C. L., 2003: *Aqua*: An Earth-observing satellite mission to examine water and other climate variables. *IEEE Trans. Geosci. Remote Sens.,* **41,** 173–184.

Partain, P., 2004: *CloudSat* ECMWF-AUX auxiliary data process description and interface control document. Cooperative Institute for Research in the Atmosphere, Colorado State University, Fort Collins, CO, 8 pp. [Available online at http://www.cloudsat.cira.colostate.edu/ICD/ECMWF-AUX/ECMWF-AUX_PDICD_3.0.pdf.]

Pincus, R., C. P. Batstone, R. J. P. Hofmann, K. E. Taylor, and P. J. Glecker, 2008: Evaluating the present-day simulation of clouds, precipitation, and radiation in climate models. *J. Geophys. Res.,* **113,** D14209, doi:10.1029/2007JD009334.

Platnick, S., M. D. King, S. A. Ackerman, W. P. Menzel, B. A. Baum, J. C. Riedi, and R. A. Frey, 2003: The MODIS cloud products: Algorithms and examples from *Terra*. *IEEE Trans. Geosci. Remote Sens.,* **21,** 459–473, doi:10.1109/TGRS.2002.808301.

Rossow, W. B., G. Tselioudis, A. Polak, and C. Jakob, 2005: Tropical climate described as a distribution of weather states indicated by distinct mesoscale cloud property mixtures. *Geophys. Res. Lett.,* **32,** L21812, doi:10.1029/2005GL024584.

Sanderson, B. M., C. Piani, W. J. Ingram, D. A. Stone, and M. R. Allen, 2008: Towards constraining climate sensitivity by linear analysis of feedback patterns in thousands of perturbed-physics GCM simulations. *Climate Dyn.,* **30,** 175–190.

Sassen, K., and J. R. Campbell, 2001: A midlatitude cirrus cloud climatology from the Facility for Atmospheric Remote Sensing: Part I: Macrophysical and synoptic properties. *J. Atmos. Sci.,* **58,** 481–496.

——, D. O'C. Starr, and T. Uttal, 1989: Mesoscale and microscale structure of cirrus clouds: Three case studies. *J. Atmos. Sci.,* **46,** 371–396.

——, Z. Wang, and D. Liu, 2008: Global distribution of cirrus clouds from *CloudSat*/*Cloud–Aerosol Lidar and Infrared Pathfinder Satellite Observations* (*CALIPSO*) measurements. *J. Geophys. Res.,* **113,** D00A12, doi:10.1029/2008JD009972.

Schmetz, J., P. Pili, S. Tjemkes, D. Just, J. Kerkmann, S. Rota, and A. Ratier, 2002: An introduction to Meteosat Second Generation (MSG). *Bull. Amer. Meteor. Soc.,* **83,** 977–992.

Schwartz, M. C., and G. G. Mace, 2010: Co-occurrence statistics of tropical tropopause layer cirrus with lower cloud layers as derived from *CloudSat* and *CALIPSO* data. *J. Geophys. Res.,* **115,** D20215, doi:10.1029/2009JD012778.

Shapiro, M. A., 1981: Frontogenesis and geostrophically forced secondary circulations in the vicinity of jet stream-frontal zone systems. *J. Atmos. Sci.,* **38,** 954–972.

——, and P. J. Kennedy, 1981: Research aircraft measurements of jet stream geostrophic and ageostrophic winds. *J. Atmos. Sci.,* **38,** 2642–2652.

Soden, B. J., 1998: Tracking upper tropospheric water vapor radiances: A satellite perspective. *J. Geophys. Res.,* **103,** 17 069–17 081.

——, and I. M. Held, 2006: An assessment of climate feedbacks in coupled ocean-atmosphere models. *J. Climate,* **19,** 3354–3360.

——, and G. A. Vecchi, 2011: The vertical distribution of cloud feedback in coupled ocean-atmosphere models. *Geophys. Res. Lett.,* **38,** L12704, doi:10.1029/2011GL047632.

Starr, D. O'C., and D. P. Wylie, 1990: The 27–28 October 1986 FIRE cirrus case study: Meteorology and clouds. *Mon. Wea. Rev.,* **118,** 2259–2287.

Stephens, G. L., 2005: Cloud feedbacks in the climate system: A critical review. *J. Climate,* **18,** 237–273.

——, and Coauthors, 2002: The *CloudSat* mission and the A-Train. *Bull. Amer. Meteor. Soc.,* **83,** 1771–1790.

——, and Coauthors, 2008: *CloudSat* mission: Performance and early science after the first year of operation. *J. Geophys. Res.,* **113,** D00A18, doi:10.1029/2008JD009982.

Waliser, D., and Coauthors, 2009: Cloud ice: A climate model challenge with signs and expectations of progress. *J. Geophys. Res.,* **114,** D00A21, doi:10.1029/2008JD010015.

Webb, M. J., and Coauthors, 2006: On the contribution of local feedback mechanisms to the range of climate sensitivity in two GCM ensembles. *Climate Dyn.,* **27,** 17–38.

Wentz, F. J., and T. Meissner, 2000: AMSR Algorithm Theoretical Basis Document (ATBD) version 2, AMSR ocean algorithm. RSS Tech. Proposal 121599A-1, 59 pp.

Wielicki, B. A., and Coauthors, 1998: Clouds and the Earth's Radiant Energy System (CERES): Algorithm overview. *IEEE Trans. Geosci. Remote Sens.,* **36,** 1127–1141.

Wilks, D. S., 2006: *Statistical Methods in the Atmospheric Sciences.* 2nd ed. Academic Press, 627 pp.

Williams, K. D., and G. Tselioudis, 2007: GCM intercomparison of global cloud regimes: Present-day evaluation and climate change response. *Climate Dyn.,* **29,** 231–250.

——, and M. J. Webb, 2009: A quantitative performance assessment of cloud regimes in climate models. *Climate Dyn.,* **33,** 141–157.

Winker, D. M., B. H. Hunt, and M. J. McGill, 2007: Initial performance assessment of CALIOP. *Geophys. Res. Lett.,* **34,** L19803, doi:10.1029/2007GL030135.

Zelinka, M. D., and D. L. Hartmann, 2010: Why is longwave cloud feedback positive? *J. Geophys. Res.,* **115,** D16117, doi:10.1029/2010JD013817.

——, S. A. Klein, and D. L. Hartmann, 2012: Computing and partitioning cloud feedbacks using cloud property histograms. Part I: Cloud radiative kernals. *J. Climate,* **25,** 3715–3735.

Zhang, Y., and G. Mace, 2006: Retrieval of cirrus microphysical properties with a suite of algorithms for airborne and spaceborne lidar, radar and radiometer data. *J. Appl. Meteor. Climatol.,* **45,** 1665–1708.

——, S. Klein, G. G. Mace, and J. Boyle, 2007: Cluster analysis of tropical clouds using *CloudSat* data. *Geophys. Res. Lett.,* **34,** L12813, doi:10.1029/2007GL029336.